

# NATIONAL ADVISORY COMMITTEE FOR AERONAUTICS

TECHNICAL NOTE 3627

BOUNDARY-LAYER GROWTH AND SHOCK ATTENUATION IN A  
SHOCK TUBE WITH ROUGHNESS

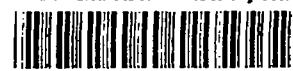
By Paul W. Huber and Donald R. McFarland

Langley Aeronautical Laboratory  
Langley Field, Va.



Washington  
March 1956

AFM 8  
TECHNICAL LIBRARY  
AFL 2311



## NATIONAL ADVISORY COMMITTEE FOR AERONAUTICS

## TECHNICAL NOTE 3627

BOUNDARY-LAYER GROWTH AND SHOCK ATTENUATION IN A  
SHOCK TUBE WITH ROUGHNESS

By Paul W. Huber and Donald R. McFarland

## SUMMARY

Measurements of unsteady-flow turbulent boundary-layer characteristics have been made for artificially thickened boundary layers using a new optical technique which involves the bow-wave shape of bullets fired in a shock tube. Comparison of the unsteady-flow boundary-layer characteristics obtained with pyramid-shaped surface roughness is made with Schlichting's flat-plate steady-flow sand-roughness theory and with steady-flow measurements reported for sand roughness and for lateral square-bar roughness.

Good agreement of the boundary-layer-thickness measurements with the steady-flow theory and with the steady-flow data was obtained. The measured velocity profiles were considerably less full than the steady-flow sand-roughness theory predicts but agreed well with steady-flow profiles which were reported for the lateral bar roughness. It is shown that these differences in profiles do not lead to any large differences in the momentum thicknesses but do lead to much larger differences in the displacement thicknesses.

Shock-wave-attenuation measurements were made in the shock tube for both smooth surfaces and surfaces of pyramid-shaped roughness of different heights and length. Comparison of the measurements with a simple attenuation theory based on equivalent flat-plate steady-flow sand-roughness boundary-layer theory is made.

The shock-wave-attenuation measurements agreed reasonably well with the theory for small values of the boundary-layer displacement thickness but the measurements were considerably lower than the theoretical values for larger values of the displacement thickness.

## INTRODUCTION

In recent years there has been an increase in the use of the shock tube as a means for the study of fluid properties and fluid flows at the high temperatures for which this research tool is particularly adaptable.

This has naturally led to a corresponding increase in the study of the departures of the real fluid flow occurring in the shock tube from the flow indicated by any particular theory. These departures have, in general, been more marked at the higher temperatures and accompanying higher flow velocities and have been attributed to a number of causes including relaxation effects, changes of the fluid properties, and effects on the fluid-flow characteristics near the walls due to heat transfer and skin friction.

The purpose of this investigation is to study the last effect, that of skin friction, by artificially increasing the magnitude of the friction through the use of surface roughness. In this manner, very thick boundary layers may be produced, and large shock-wave attenuations noted. Direct observations of the boundary-layer characteristics are made with a new optical technique which involves study of the bow-wave shape from a bullet fired in the shock tube. The shock-wave attenuations which are obtained with the use of surface roughness are of such magnitude that the troublesome effects of imperfect diaphragm burst and instrumentation inaccuracies are reduced to second order.

A review of the shock-tube literature shows that the aerodynamics of the real shock-tube flow in certain cases might be very different from that expected from the ideal theory. (See, for example, ref. 1 for treatment of the ideal shock-tube theory.) It was found in references 2 to 4 that regions of flow in the shock tube which would otherwise have conditions constant in time exhibit continuous variation of pressure, density, and Mach number with time. Changes of the shock-wave strength and other flow parameters with distance traversed and with shock-tube pressure ratio, Reynolds number, and so forth are noted in references 1, 5, 6, and 7. Theoretical and experimental studies have been made to correlate experimentally obtained shock-tube flow measurements with viscous unsteady-flow theory. In these studies the wall boundary conditions are included by considering the flow as a quasi-one-dimensional flow, where the flow conditions are averaged across the channel at representative cross sections along the shock tube and the resulting values included in a one-dimensional theory.

In references 1 and 5, one representative cross section was chosen, that being at the entropy discontinuity, and the mass-flow decrement at this cross section, as a result of the boundary-layer displacement thickness, was presumed to be equal to the mass-flow decrement at the shock wave at the same time. The displacement thickness was determined according to the Rayleigh laminar problem of the instantaneous acceleration to constant velocity of a flat plate in a fluid at rest.

In an investigation (unpublished) at the Langley Aeronautical Laboratory in 1953, the authors collaborated on a theory which, like references 1 and 5, used the mass-flow decrement due to the boundary-layer

displacement thickness at the discontinuity as the characteristic parameter. This mass-flow decrement, however, was assumed to equal the shock-wave mass-flow decrement which existed at a later time, this time being equal to the time required for a sonic wave to travel from the discontinuity to the shock. The displacement thickness was determined from flat-plate steady-flow turbulent empirical data at a flat-plate length corresponding to the flow distance from the diaphragm to the discontinuity.

In reference 2, a theory was developed in which the entire hot-gas region between the entropy discontinuity and shock wave was represented as a quasi-steady flow by the choice of a coordinate system fixed to the shock. The Blasius laminar-boundary-layer solution was applied with the wall velocity nonzero, and the changes of momentum and energy due to skin friction and heat transfer were thus obtained. It was assumed that these effects resulted in the generation of waves which could overtake the shock and reduce its strength.

An inclusive treatment of the shock-tube flow for the viscous, heat-conducting case has been done in reference 4 in which the complete flow in the shock tube is considered. Numerical evaluation of this theory is obtained by assuming that, at any point on the shock-tube wall, the drag and heat transfer are equal to the flat-plate steady-flow values at a distance from the leading edge of the plate equal to the shock-tube-flow distance at that point. The flow quantities in the boundary layer are averaged into the free-stream flow; by integration of the unsteady-flow-characteristics differential equations, including some linearizations, the flow parameters at any point or at any time in the shock-tube flow may be found. This method is such that any skin-friction curve - either laminar, turbulent, or combinations thereof - may be used. The first-order effects at the entropy discontinuity are also included. The treatment of the expansion fan timewise, however, was as a discontinuous front, although, for the pressure ratios covered by the experimental phase of the work, this treatment produced no large discrepancies (that is, 1.94 to 3.58 shock-wave pressure ratios).

In the aforementioned theoretical treatments the correlation of experimental and theoretical results was, in some cases, not particularly good and, in the other cases, only a rather narrow range of shock strengths was covered experimentally. In all cases, the boundary-layer displacement thickness was assumed to be small in comparison with the shock-tube cross section so that effects of streamwise pressure gradient on the boundary-layer development could be neglected along with any effects of area change on the shock-tube flow.

In references 2 and 8, the correct treatment of the boundary layer for unsteady laminar boundary layers was used. It was shown that, for the laminar case, equivalent steady-flow flat-plate treatment would not

yield correct results nor would the Rayleigh treatment in the case of finite-strength shocks. There have been, however, no solutions for the unsteady turbulent-boundary-layer case; thus, the validity of an equivalent flat-plate representation is not known.

It is felt that, by the present investigation, information may be obtained as to the validity of assumptions such as the equivalence of unsteady boundary layers to steady-flow flat-plate representations and the effect of thick boundary layers on the shock-tube flow. It is recognized, of course, that large surface roughness disallows the existence of a laminar boundary layer and, in fact, the turbulent skin-friction dependency on Reynolds number is absent under most of the conditions encountered in the investigation. It is felt, however, that some fundamental information as to unsteady-flow boundary-layer development may be obtained, despite this limitation, by comparing the resulting information with steady-flow flat-plate theory with these same limitations.

#### SYMBOLS

a	velocity of sound
A	cross-sectional area
b	shock-tube width
$c_f$	local skin-friction coefficient
$C_f$	total skin-friction coefficient
D	shock-tube perimeter
F	bow-wave parameter, $\frac{2}{\gamma - 1} \left( \frac{\sin i}{M_n} \right)^2$
h	shock-tube height
i	bow-wave incidence angle
k	roughness size
$k^*$	height above surface of a hypothetical wall which would give a shock-tube area reduction equal to average reduction due to roughness
l	distance shock has traveled from leading edge of surface to midpoint of velocity-measurement section

M	fluid-flow Mach number
N	reciprocal of velocity exponent in boundary layer, $\frac{u(y)}{u_{\infty}} = \left(\frac{y}{\delta}\right)^{1/N}$
p	absolute pressure
R	Reynolds number based on flow length, $R = \frac{ux}{\nu}$
$R_{ks}$	Reynolds number based on sand roughness size, $\frac{uk_s}{\nu}$
t	time
T	absolute temperature
u	fluid-flow velocity
$u_{\tau}$	shearing-stress velocity in boundary layer
$V_1$	shock-wave velocity
x	fluid-flow distance
y	distance from wall normal to flow
$\gamma$	ratio of specific heats
$\delta$	boundary-layer thickness
$\delta^*$	incompressible boundary-layer displacement thickness (eq. (25))
$\theta$	incompressible boundary-layer momentum thickness (eq. (14))
$\lambda$	roughness equivalence factor (eq. (18))
$\mu$	Mach angle
$\nu$	kinematic viscosity
$\rho$	density
$\phi_w$	wall-temperature coefficient, $\frac{1 - \frac{T_w}{T_2}}{\frac{\gamma - 1}{2} M_2^2}$

## Subscripts:

0	high-pressure side of shock tube before burst
1	low-pressure side of shock tube before burst
2	region between shock-wave and entropy discontinuity
$\infty$	free stream outside of boundary layer (as used herein is always that of region 2)
a	relative to fluid
B	bullet
n	normal to bow wave
rw	rough wall
s	sand roughness form
saw	saw profile roughness form
sw	smooth wall
t	total adiabatic
w	wall
$\sigma$	immediately behind bow wave

## THEORY

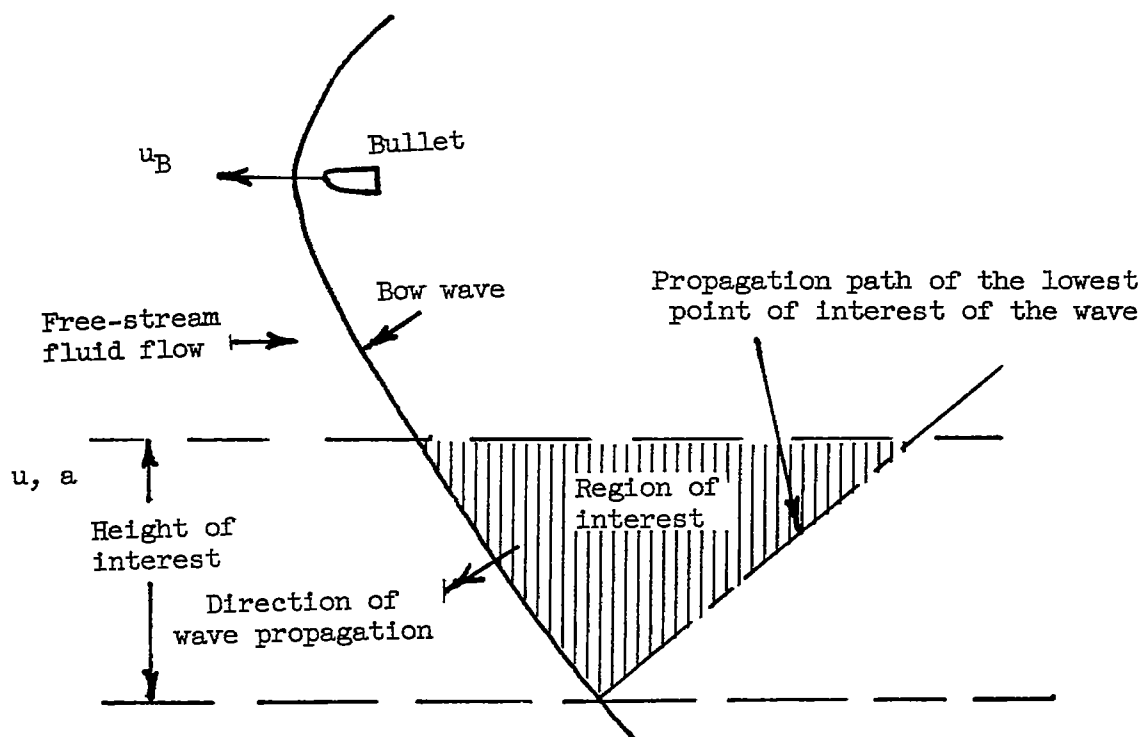
## Bullet Theory

The method usually adopted in steady flows for the determination of boundary-layer velocity profiles is the survey of this region by small pitot-static probes. This method is not adaptable, however, to unsteady flows since rapid-response gages of sufficiently small size are at present not obtainable. The use of an optical technique is desirable in general since the flow is not disturbed and photographs may be obtained at prescribed times. An interferometer could be used to determine density profiles and (for the case of constant static pressure) temperature profiles provided that refraction effects near the wall are sufficiently small to allow analysis of the records. In order to obtain velocity profiles, however, this method would depend directly on knowledge of the temperature-velocity relation in the boundary layer. The optical technique which is here set forth using bullets also requires

this knowledge of the temperature-velocity relation, but the results are not directly dependent upon the relation. The use of the bullet method also requires knowledge of the bullet bow-wave strength in the boundary layer, but it will be shown that lack of this knowledge may not be serious in many cases.

If a bullet is moving supersonically with respect to a fluid, the disturbance, or shock wave, from the nose propagates out into the fluid and the path, or shape of this bow wave, is a history of the strength of the bow wave and of the fluid velocity and temperature (that is, fluid Mach number) through which it has propagated. If the wave should, at any point, encounter conditions tending to make the wave speed become subsonic with respect to the fluid, the shape is dependent also on time and eventually the wave disappears. In order, therefore, that interpretation of the bow-wave shape might be made in terms of velocity and temperature changes, the restriction of supersonic wave speed at all points is imposed and the change in wave strength must be known.

Consider a bullet which is fired into a fluid in a direction opposite to the fluid flow (see following sketch):





The Mach number of the bullet with respect to the fluid is

$$M_a = \frac{u + u_B}{a} \quad (1)$$

If streamwise variations in the fluid flow may be considered small in comparison with changes normal to the fluid flow, the Mach number normal to the wave is

$$M_n = M_a \sin i \geq 1.0 \quad (2)$$

(It should be here noted that the wave incidence angle is a measure of the ratio of normal Mach number (wave strength) to the Mach number of the wave relative to the fluid only within certain limitations in unsteady flow, these limitations being that no gradients of  $u$  or  $a$  in the direction of flow be present within the region of interest. This region of interest (see preceding sketch) is that region bounded by the wave on the one side and by the propagation path of the lowest point of interest of the wave on the other side. If these conditions are respected, the incidence angle will then be a measure of the aforementioned ratio in the presence of gradients of  $u$  and  $a$  normal to the flow.)

If it can be assumed that the wave is very weak - that is, a Mach wave where  $\frac{p_0}{p_\infty} = 1.0$  - or if the wave strength is known,  $M_n$  is determined since

$$M_n^2 = \frac{\gamma - 1}{2\gamma} \left( \frac{\gamma + 1}{\gamma - 1} \frac{p_0}{p_\infty} + 1 \right) \quad (3)$$

If the wave strength is not known in the region of interest, some assumed variation of wave strength from a known point outside the region must be used. For example, the wave-strength variation in the free stream is known from determination of the wave angle,  $u_B$ ,  $u_\infty$ , and  $a_\infty$ , and this variation may be assumed to extrapolate into the region of interest.

The bullet velocity  $u_B$  is measured experimentally and the shock angle  $i$  is measured from schlieren photographs; thus, there are two remaining unknowns  $u$  and  $a$  and it is necessary to find an additional relationship. The relationship between the velocity and temperature in the boundary layer may be determined for particular cases.

The simplest assumed relation between velocity and temperature in the boundary layer - for the case of no heat transfer at the wall and a Prandtl number of 1 - is used so that, according to the energy equation, the relation between velocity and temperature in the hot-gas region may be written

$$\frac{T}{T_2} = \frac{T_{2,t}}{T_2} - \frac{T_{2,t} - T_2}{T_2} \left( \frac{u}{u_2} \right)^2 \quad (4)$$

For the purpose of finding the influence of this assumption of no wall heat transfer on the results, the velocity-temperature relation for the turbulent case of a Prandtl number of 1, including heat transfer from the wall, will also be used for comparison. According to Crocco (ref. 9), this relationship may be expressed as

$$\frac{T}{T_2} = \frac{T_w}{T_2} - \frac{T_{2,t} - T_2}{T_2} \left( \frac{u}{u_2} \right)^2 + \frac{T_{2,t} - T_w}{T_2} \frac{u}{u_2} \quad (5)$$

which for the boundary condition  $T_{2,t} = T_w$  is identical to equation (4). For this unsteady case, however, the condition  $T_w = T_1$  is used. Equation (5) is for the case of constant wall temperature and no streamwise pressure gradients.

It is now possible to find the velocity at any point in the flow in terms of the bow-wave angle at that point if the wave strength is also known at that point. By combining equations (1), (2), and (4), the solution for the velocity may be expressed nondimensionally for the case in which there is no heat transfer from the wall as

$$\frac{u}{u_2} = \frac{-2F \frac{u_B}{u_2} + \sqrt{\left(2F \frac{u_B}{u_2}\right)^2 - 4(F+1) \left[ F \left( \frac{u_B}{u_2} \right)^2 - 1 - \frac{2}{(\gamma-1)M_2^2} \right]}}{2(F+1)} \quad (6)$$

where

$$F = \frac{2}{\gamma-1} \left( \frac{\sin i}{M_n} \right)^2$$

By combining equations (1), (2), and (5), the solution for the velocity may similarly be expressed for the turbulent case of heat transfer from the wall only as

$$\frac{u}{u_2} = \frac{\phi_w + 1 - 2F \frac{u_B}{u_2} + \sqrt{\left(\phi_w + 1 - 2F \frac{u_B}{u_2}\right)^2 - 4(F+1) \left[F \left(\frac{u_B}{u_2}\right)^2 + \phi_w - \frac{2}{(\gamma-1)M_2^2}\right]}}{2(F+1)} \quad (7)$$

where

$$\phi_w = \frac{1 - \frac{T_w}{T_2}}{\frac{\gamma-1}{2} M_2^2}$$

For the case in which there is no heat transfer from the wall, a value of -1 for  $\phi_w$  makes equation (7) again identical to equation (6).

#### Boundary-Layer-Growth Theory

Smooth plate.- For the purpose of determining a theoretical boundary-layer growth with which experimental measurements may be compared, as well as for later use in a simple attenuation theory, the equivalent steady-flow concept without heat transfer or pressure drop will be used. That is, flat-plate steady-flow turbulent-boundary-layer theory will be used where the flow length  $x = ut$  in the shock tube is equivalent to the flat-plate length.

If the initial assumption is made that the flow is turbulent from the leading edge of a plate and that the velocity distribution remains constant along the plate, or more specifically that  $\theta/\delta$  is constant, the boundary-layer growth along the plate may be readily determined in terms of the local skin-friction coefficient. (See, for example, refs. 10 and 11.)

$$d\delta(x) = \frac{1}{2} \frac{\delta}{\theta} c_f dx \quad (8)$$

If the velocity distribution in the boundary layer is of the power form

$$\frac{u(y)}{u_\infty} = \left(\frac{y}{\delta}\right)^{1/N} \quad (9)$$

the local skin-friction coefficient for a smooth plate for Reynolds numbers in the range  $5 \times 10^5 < R < 10^7$  is found from reference 10 to be

$$c_f = 0.059R^{-2/(3+N)} \quad (10)$$

where  $N = 7$ .

By substituting equation (10) into equation (8) and integrating from 0 to  $x$ , the boundary-layer growth along the smooth plate is found in terms of the total skin-friction coefficient:

$$\delta(x) = \frac{1}{2} \frac{\delta}{\theta} x C_f \quad (11)$$

where (see ref. 11)

$$C_f = c_f \frac{3 + N}{1 + N} \quad (12)$$

A plot of the total skin-friction coefficient as a function of Reynolds number based on plate length according to equation (12) is given in figure 1. This curve is seen to approximate closely the smooth-plate skin-friction value of reference 10 shown as the lower dashed line.

Equation (11) may be expressed numerically for  $N = 7$  in terms of the flow length  $x$ :

$$\delta(x) = 0.38xR^{-1/5} \quad (13)$$

since

$$\frac{\theta}{\delta} = \frac{N}{(N+1)(N+2)} = \frac{1}{u_\infty^2} \int_0^1 u(u_\infty - u) d\frac{y}{\delta} \quad (14)$$

with the assumption of low-velocity (incompressible) flow.

Rough plate.— For fully developed roughness flow along a flat plate, that is, flow in which the roughness projects out of the laminar sub-layer, the steady-flow friction drag consists primarily of the drag of the individual roughness elements. In this case, the skin friction is independent of Reynolds number and for values of the characteristic

roughness number  $\frac{u_\tau k_s}{\nu} \geq 70$  is given by

$$C_f = \left( 1.89 + 0.704 \log_e \frac{x}{k_s} \right)^{-2.5} \quad (15)$$

(See ref. 10 for complete treatment of roughness flow over plates as transformed from Nikuradse's (ref. 12) measurements on pipes with sand roughness.)

The velocity distribution for this case of fully developed roughness is assumed to be the same as that in Nikuradse's pipe and is given by

$$\frac{u}{u_\tau} = 2.5 \log_e \frac{y}{k_s} + 8.5 \quad (16)$$

The above expression for total skin-friction coefficient (eq. (15)) is shown in figure 1 and the velocity distribution (eq. (16)) is shown in figure 2. Note that the roughness skin friction in figure 1 is also shown as a function of flow Reynolds number for given values of the roughness Reynolds number  $R_{ks}$ . (It is seen from fig. 2 that the Schlichting velocity distribution is very closely approximated over much of the range of  $\frac{y}{k_s}$  by an  $N = 5.5$  power velocity profile except for the region close to the roughness.)

Equation (16) may also be expressed as

$$\frac{u}{u_\infty} = \frac{u_\tau}{u_\infty} 2.5 \log_e \frac{y}{\delta} \frac{\delta}{k_s} + 8.5 \frac{u_\tau}{u_\infty} \quad (17)$$

Roughness other than sand may be used, however, with the same relations if an equivalent sand-roughness size is determined from

$$k_s = \lambda k \quad (18)$$

where  $k$  denotes the arbitrary roughness size and the factor  $\lambda$  prescribes an equivalent sand size as used by Nikuradse to produce the same friction as that produced by  $k$ . (See ref. 13 for comparison of friction measurements of other roughness forms with sand.)

The boundary-layer growth along the rough plate for fully developed sand roughness is found from substitution of equation (15) into equation (11):

$$\frac{\delta}{k_s} = \frac{1}{2} \frac{\delta}{\theta} \frac{x}{k_s} \left( 1.89 + 0.704 \log_e \frac{x}{k_s} \right)^{-2.5} \quad (19)$$

Numerical evaluation of  $\frac{\delta}{k_s}$  as a function of  $\frac{x}{k_s}$  is now obtained by first assuming a value of  $\frac{\delta}{k_s}$  in equation (17) and solving for  $\frac{u_\infty}{u_\tau}$  at the edge of the boundary layer. If these values of  $\frac{u_\infty}{u_\tau}$  and  $\frac{\delta}{k_s}$  and equation (17) are used,  $\frac{\theta}{\delta}$  may be found from integration of equation (14). Equation (19) can then be plotted in the form of

$$2 \left( \frac{\delta}{k_s} \frac{\theta}{\delta} \right) = \frac{x}{k_s} \left( 1.89 + 0.704 \log_e \frac{x}{k_s} \right)^{-2.5}$$

against  $\frac{x}{k_s}$  and may be used to find  $\frac{x}{k_s}$ ,  $\frac{\theta}{\delta}$  and  $\frac{\delta}{k_s}$  being known. This function, which is the growth of the momentum thickness along the plate, is plotted in figure 3.

It is recognized that equation (19) was obtained on the basis of a velocity distribution along the plate invariant with  $x$  and that this qualification does not hold for the case of roughness. (See eq. (17).) Since the change in velocity distribution along the plate has only a small influence in this case (see fig. 4 for influence of  $\frac{\delta}{k_s}$  on  $\frac{\theta}{\delta}$  according to the Schlichting theory), equation (19) is justifiable in view of some of the other assumptions which are made.

#### Shock-Attenuation Theory

A simple shock-attenuation theory will be developed for comparison with experimental results. It is similar to those of references 1 and 5 in that the mass-flow decrement due to the boundary-layer displacement thickness at the entropy discontinuity will be presumed equal to the shock-mass-flow decrement at the same time. The theory is different, however, in that the boundary-layer displacement thickness will be based on the equivalent flat-plate steady-flow value for a plate of length equal to the shock-tube-flow length in the same manner as was done for the boundary-layer growth.

The reduction of shock-tube cross section at any location due to the boundary-layer displacement thickness is

$$\frac{\Delta A}{A} = \frac{\delta^*(D - 4\delta^*)}{A} \quad (20)$$

where  $D = 2b + 2h$  is the shock-tube perimeter and  $A$ , the cross-sectional area.

When  $4\delta^* \ll D$ , equation (20) reduces to

$$\frac{\Delta A(\delta^* \ll D)}{A} = \frac{\delta^* D}{A} \quad (21)$$

which is applicable when the displacement thickness is small in comparison with the shock-tube cross-sectional dimensions. When this is not the case, the error in area reduction by using equation (21) would be

$$\frac{\Delta A(\delta^* \ll D)}{\Delta A} - 1 = \frac{1}{\frac{D}{4\delta^*} - 1} \quad (22)$$

If the free-stream conditions are assumed to be unaltered by the presence of the boundary layer, the fractional mass-flow reduction is then equal to the fractional area reduction:

$$\frac{A(\rho_2 u_2)}{\rho_2 u_2} = \frac{\Delta A}{A} \quad (23)$$

In order to convert the mass-flow reduction to shock-wave attenuation, it is assumed that the mass flow is reduced at the shock wave by the same fraction of the total as it is at the entropy discontinuity. (The wave mechanism by which this mass-flow reduction is accomplished is not considered, but the net effect would be that of expansion waves generated at the wall which would in turn overtake the shock wave.) The mass flow per unit area accelerated by the shock wave is nearly a linear function of the shock-pressure ratio (see fig. 5); thus, the

shock-pressure attenuation is simply expressed for small values of  $\delta^*$  by

$$\frac{\frac{\Delta \frac{p_2}{p_1}}{\frac{p_2}{p_1} - 1}}{\frac{p_2}{p_1} - 1} = \frac{\Delta(\rho_2 u_2)}{\rho_2 u_2} = \delta^* \frac{D}{A} \quad (24)$$

For the smooth-wall incompressible turbulent boundary layer with a power-law velocity profile, the ratio of  $\delta^*$  to  $\delta$  is found from

$$\frac{\delta^*}{\delta} = \frac{1}{u_\infty} \int_0^1 (u_\infty - u) \, d \frac{y}{\delta} = \frac{1}{N+1} \quad (25)$$

so that substitution of equations (25) and (13) into equation (24) for  $N = 7$  yields

$$\frac{\frac{\Delta \frac{p_2}{p_1}}{\frac{p_2}{p_1} - 1}}{\frac{p_2}{p_1} - 1} = \frac{0.38}{8} \frac{D}{A} \left( \frac{v_2}{u_2 x} \right)^{1/5} x \quad (26)$$

and from the shock-tube  $x$ - $t$  diagram (see fig. 6(a))

$$x = \frac{x}{l} l = \frac{u_2}{V_1} l \quad (27)$$

Equation (26) may now be rewritten as a shock-pressure attenuation coefficient:

$$\frac{4 \frac{A}{D} \frac{\frac{\Delta \frac{p_2}{p_1}}{\frac{p_2}{p_1} - 1}}{\frac{p_2}{p_1} - 1}}{\left( \frac{v_1}{a_1} \right)^{0.2} (l_{sw})^{0.8}} = 0.19 \frac{\left( \frac{u_2}{V_1} \right)^{0.8}}{\left( \frac{R}{x} \right)^{0.2} \left( \frac{v_1}{a_1} \right)^{0.2}} \quad (28)$$



The right-hand side of equation (28) is a function only of shock-pressure ratio and initial temperature in the shock tube.

For the rough-wall case the ratio of  $\delta^*$  to  $\delta$  may be found by integration of equation (25) after substitution of equation (17) for the assumed values of  $\frac{\delta}{k_s}$ , as was done in the case of  $\frac{\theta}{\delta}$  previously.

Substitution of equation (19) into equation (24) yields

$$\frac{\Delta \frac{p_2}{p_1}}{\frac{p_2}{p_1} - 1} = \frac{k_s}{2} \frac{\delta^*}{\delta} \frac{\delta}{\theta} \frac{D}{A} \frac{x}{k_s} \left( 1.89 + 0.704 \log_e \frac{x}{k_s} \right)^{-2.5} \quad (29)$$

for the shock-pressure attenuation, and this may be expressed as a shock-pressure-attenuation coefficient by

$$\frac{\frac{A}{D} \frac{\Delta \frac{p_2}{p_1}}{\frac{p_2}{p_1} - 1}}{\frac{l_{rw}}{l_{rw}} \frac{p_2}{p_1} - 1} = 2 \frac{\delta^*}{\delta} \frac{\delta}{\theta} \frac{u_2}{V_1} \left( 1.89 + 0.704 \log_e \frac{u_2}{V_1} \frac{l_{rw}}{k_s} \right)^{-2.5} \quad (30)$$

The right-hand side of equation (30) is a function only of the shock-pressure ratio and the ratio  $\frac{l_{rw}}{k_s}$ . Here again, the velocity distribution along the plate is not constant as the derivation requires, and the influence on  $\frac{\delta^*}{\delta}$  is more pronounced than it was on  $\frac{\theta}{\delta}$  (see fig. 4); thus, the error in attenuation will be more pronounced than was the error in boundary-layer thickness.

#### APPARATUS AND PROCEDURE

Studies of the boundary-layer growth and shock-wave attenuation were made in a stainless-steel shock tube 4 inches wide and  $7\frac{1}{2}$  inches high with a maximum length of 22 feet. A schematic arrangement of the experimental apparatus is shown in figure 7. The high-pressure side of the shock tube in this investigation was 4 feet long and pressures up

to 100 pounds per square inch were used. The low-pressure side consisted of interchangeable sections of 2-foot, 4-foot, and 8-foot lengths and of two sections each of 2-foot lengths, these latter sections containing 8- by 16-inch plate-glass windows  $1\frac{1}{4}$  inch thick. The sections were doweled for accurate alinement and connected with quick-acting clamps. The low-pressure side was at atmospheric pressure for shock pressure ratios up to about 2.5 and was lowered to about 0.1 atmosphere for the highest pressure ratios used.

The smooth-wall attenuation study was made first after which the 2-foot window sections were equipped with roughness on only the lower wall for the optical investigation using bullets. Finally, either the 8-foot or 4-foot sections were alternately lined with roughness of three different grades on all four walls for the rough-wall attenuation studies. The roughness consisted of plastic sheets which were machined on the surface to form continuous rows of pyramid-shaped elements of square base and of height equal to one-half of the base dimension. The pyramids completely covered the surface and the rows were oriented at  $45^\circ$  to the flow direction. (See fig. 7.) Three sizes of roughness were used but in each case the overall thickness of the plastic was such that the reduction of shock-tube cross-sectional area was the same for all three sizes. Smooth sheets of such thickness as to give this same area reduction were also used to line the 8-foot section in one series of tests to determine the effect of this area reduction on the shock-tube flow. All the sheets had  $45^\circ$  beveled side edges for fitting in the shock tube and were cemented tightly to the shock-tube walls.

Shock velocities were measured by means of an electronic chronograph and two pickup stations were used to start and stop the chronograph. The pickups were located 18 inches apart in the 2-foot section and were commercial piezoelectric-type gages connected to the shock tube through slit-shaped openings on the walls of the shock tube. It was felt that this arrangement would minimize the voltage-rise time at shock passage since this rise time varies with the dimension of the opening in the flow direction. For the smooth-wall studies, the midway point of the gages was 13 feet from the diaphragm; for the rough-wall studies, the midway point was 1 foot downstream of the section containing the roughness. Records of pressure against time were obtained at the midpoint of the velocity gages in a few tests using capacitive-type flush-mounted pickups along with a cathode-ray oscilloscope and drum camera.

For the bullet investigation of the boundary layer, 22-caliber "long rifle" and "Hornet" bullets were fired upstream (toward the high-pressure end) through a hole in the end plate of the low-pressure section. A paper diaphragm could be placed over the hole for evacuation purposes. The bullet speed could be approximately predetermined by the charge loading and, by means of pickups and delay circuits strategically placed, the

bullet speed could be electronically determined and synchronization of the optical light source with the bullet and shock-tube shock wave was possible.

The optical components included a high-voltage spark-light source, thyratron controlled, and a two-mirror schlieren system using front-surfaced, 16-inch-diameter, parabolic mirrors. The spark duration was about 1 microsecond and there was sufficient light to expose a 5- by 7-inch sheet of fast panchromatic film.

The shock-tube diaphragm consisted of one or more sheets of exposed film so that the diaphragm would be stressed nearly to the bursting point and firing was accomplished with a solenoid-actuated trigger unit. The shock-tube temperature was determined prior to each run.

## RESULTS AND DISCUSSION

### Boundary-Layer Measurements

Boundary-layer measurements were made with the bullet technique for two values of flow length over roughness and for two values of shock-tube pressure ratio (that is, flow velocity). The shock-tube configurations used for this investigation are shown in table I. It was necessary that proper synchronization of the shock tube, gun, and light source be accomplished so that the bullet would be within the "roughness-flow region" at the time of the photograph. That is, the photograph was taken at a time before any flow from the smooth region ahead of the roughness could reach the position under investigation (see fig. 6(b)) as well as before the shock reflected from the end plate could reach this position. The actual flow length appropriate to each photograph could then be determined from the  $x$ - $t$  diagram using the reflected shock from the end plate as a reference point. The shock-tube flow was known from shock-velocity measurements. A photograph typical of those obtained using this method is shown in figure 8(a). In order to determine the velocity profile from equation (6) or (7), it is necessary to know the Mach number normal to the bow wave or the bow-wave strength at each ordinate. The bow wave is nearly a Mach wave in the region of the boundary layer in these tests and its strength is closely determined outside the boundary layer from measurements of bow-wave incidence angle and the known bullet speed and free-stream conditions. (See eqs. (1), (2), and (3).) A plot of  $M_n$  as a function of distance from the bullet is then extrapolated into the region of the boundary layer. The coordinate system used in plotting the boundary-layer measurements is shown in figure 9 where the  $y = 0$  point is taken at the ordinate corresponding to a smooth plane of equal shock-tube-area reduction. This system is also used in reference 13. A plot of bow-wave incidence angle minus Mach angle near a rough wall as measured from a typical photograph (fig. 8(a)) is shown in figure 10. It can be seen from figure 10 that

the edge of the boundary layer is readily determined in this case from the point at which the slope of the bow wave changes more or less discontinuously. It was found in many of the photographs, however, that the bow wave was distorted as a result of interactions with one or more of the many weak reflections persisting in the field, these reflections having originated from the initial shock-wave movement over the roughness elements. (See fig. 8(b).) These distortions might appear anywhere along the bullet bow wave and, unfortunately, led to uncertainties in the analysis of the records. Selection of a more random type of roughness would probably have reduced this effect.

In order that comparisons of the boundary-layer measurements might be made with the Schlichting theory, it is necessary to establish an equivalence of the roughness used to sand roughness. The theory outlined in Schlichting for a flat plate is based on measurements made by Nikuradse in pipes using sand roughness. For a roughness of different form and distribution from that of Nikuradse's sand roughness, the equivalence of the two must be determined from friction measurements, as was done in reference 13 for many different types of roughness. Since the friction was not measured in this case, it was necessary to assume arbitrarily an equivalence criterion based on some physical concept even though there is no physical significance to the ratio  $\lambda$  in equation (18). It was, therefore, assumed that surface roughnesses of arbitrary form and distribution would be equivalent on the basis of equal shock-tube-area reduction. From friction measurements given in reference 13, the equivalence of a saw profile roughness and Nikuradse's sand roughness was found to be  $\frac{4}{3}$  (that is,  $\lambda_{\text{saw}} = \frac{4}{3}$ ) so that

$$k_{\text{saw}}^* = \frac{1}{2} k_{\text{saw}} = \frac{1}{2} \frac{k_s}{\lambda_{\text{saw}}} \quad (31)$$

The displacement thickness for the pyramid roughness used here is given by

$$k^* = \frac{1}{3} k \quad (32)$$

and, by using the assumed equivalence criterion, the pyramid equivalence is found by equating equations (31) and (32) to yield

$$k_s = \frac{8}{9} k \quad (33)$$

With the equivalence factor  $\lambda = \frac{8}{9}$ , the boundary-layer-thickness measurements obtained with the pyramid roughness are plotted in figure 11 along with the Schlichting theoretical values from equation (19). The agreement of the average of the experimental boundary-layer-thickness measurements with the theory is good although there is a noticeable scatter of the individual data points due to the aforementioned waves in the flow field.

For comparison of these results with some steady-flow measurements obtained by using pitot-static survey probes, the results of Klebanoff and Diehl (ref. 14) for commercial sand roughness and of Moore (ref. 15) for lateral square bars are also plotted in figure 11. The equivalence of the Moore roughness form to Nikuradse sand roughness was taken as  $\frac{2}{3}$  (that is,  $\lambda = \frac{2}{3}$ ) and was determined by the same method as was used for the pyramids previously. The data of references 14 and 15 have been plotted by using the ordinate measured from  $y = 0$  at the plane of equal average channel-area reduction. The agreement of the unsteady-flow boundary-layer-thickness measurements with those values of references 14 and 15 for steady flow is good but generally the points are lower than the theoretical values. It should be pointed out that a change in the roughness equivalence factor  $\lambda$  would have only a relatively small effect on the comparison of the data with theory in figure 11. The values taken from reference 15 are for the roughness size closest to that used here. It was found in reference 15 that there was a slight dependence of the results on Reynolds number; this dependence, of course, is inconsistent with the sand-roughness theory.

#### Velocity-Profile Measurements

Boundary-layer velocity profiles over roughness were obtained from the bullet photographs and considerable scatter of the measurements was found as a result of the waves in the field, the influence being the most serious for the velocity profiles since few photographs were obtained without waves somewhere within the boundary layer. The average of the measurements taken at  $x_{rw} \approx 3$  feet is plotted in figure 12 along with the theoretical distribution for this value of  $\frac{\delta}{k_s}$ , as determined from equation (17). The experimental results were computed from equation (6). Also, for comparison, in figure 12 are plotted the steady-flow distributions found by Klebanoff and Diehl for commercial sand roughness and by Moore for lateral square bars at about the same values of  $\frac{\delta}{k_s}$ . The steady-flow data are plotted using the  $y = 0$  point at the plane of equal channel-area reduction as was used for the reported data. It is seen in figure 12 that the boundary-layer velocity profile is somewhat less full for the pyramid and lateral-bar data (ref. 15) than for the sand-roughness case of reference 14, but that all

the experimental profiles are less full than the Schlichting theory predicts. Here again the influence of the roughness equivalence factor is very small.

The most significant result appears to be that the non-sand roughness forms show a distinctly different profile from that of sand roughness although there is no apparent difference between the non-sand steady-flow and unsteady-flow profiles. In figure 13, the unsteady-flow data taken at  $x_{rw} \approx 1$  foot are plotted in the same manner and compared with the Schlichting theory and the lateral-bar data of reference 15 for the same value of  $\frac{\delta}{k_s}$ . Here again, the two non-sand profiles are very nearly the same although they are both less full than the Schlichting sand theory predicts. When the experimental unsteady-flow profiles were computed by using equation (7), the results showed an even less full profile and gave a zero velocity at the peak of the roughness rather than at  $\frac{1}{3} k$ ; therefore, these results were not used.

The profiles of figures 12 and 13 result in considerably larger experimental values of  $\delta^*$  than are predicted by the Schlichting theory as shown in figure 11. The experimental values shown result from integration of the profiles in figures 12 and 13 according to equation (25). The Schlichting theoretical curve for  $\frac{\delta^*}{k_s}$  is obtained by using figure 4.

#### Attenuation Measurements

Shock-speed measurements including both smooth-wall and rough-wall studies were made by using the shock-tube configurations shown in table I. For each shock-speed measurement recorded, a shock-strength calculation was made from one-dimensional unsteady-flow shock theory, the measured room temperature being used and a value of  $\gamma = 1.40$  being assumed. For each shock-tube diaphragm burst the pressures on each side of the diaphragm were determined immediately prior to the rupture; from this shock-tube

pressure ratio  $\frac{p_0}{p_1}$ , an initial ideal shock strength  $\frac{p_2}{p_1}$  was determined

by using ideal shock-tube theory and  $\gamma = 1.40$ . The difference between this initial shock strength and the shock strength determined from the velocity measurements is then considered as the shock loss due to the boundary layer only and is

$$\Delta \frac{p_2}{p_1} = \frac{\Delta p_2}{p_1}$$

and the shock-pressure attenuation is

$$\frac{\Delta \frac{p_2}{p_1}}{\frac{p_2}{p_1} - 1}$$

For the purpose of determining a flow length  $x$  appropriate to each measurement for use in evaluation of the theory (see eqs. (26) and (29)), equation (27) is used where  $l$  is taken as the distance the shock has traveled from the leading edge of the surface under investigation to the midpoint of the velocity measurement section. (See table I.) The value of  $\frac{x}{l}$  is determined from the  $x$ - $t$  diagram as the ratio of the distance a flow particle has traveled from the leading edge of the particular surface to the distance that the shock has traveled from this leading edge during the same time. From ideal shock-tube theory this ratio is

$$\frac{x}{l} = \frac{u_2}{V_1} = \frac{\frac{2}{\gamma - 1} \left( \frac{p_2}{p_1} - 1 \right)}{\frac{\gamma + 1}{\gamma - 1} \frac{p_2}{p_1} + 1}$$

and is plotted in figure 14 for  $\gamma = 1.40$ .

Shock-pressure-attenuation coefficients were experimentally obtained for the last five configurations listed in table I from the left-hand side of equations (28) and (30) and the theoretical attenuation coefficients were obtained from evaluation of the right-hand side of equations (28) and (30) for the same  $\frac{k_g}{k}$  as before. The results for the smooth-wall configuration are plotted in figure 15 and for the roughness configurations, in figures 16 to 19, all as a function of initial shock-wave strength. The solid arrows indicate the range of the root-mean-square deviation of the experimental data from the faired curve. The dashed arrows indicate the total range of deviation to be expected as a result of a 5-microsecond error in time measurement in the velocity measurement section. The effect of poor diaphragm bursts on the data shown is not known but the influence of this factor on the smooth-wall data of figure 15 would be much more pronounced than on the rough-wall data, since the magnitude of the shock loss due to skin friction is of a different order. The same condition is seen to be true in the case of influence of errors in time measurement on the attenuation data.

The smooth-wall results shown in figure 15 are also representative of one series of tests not listed in table I in which smooth sheets 8 feet long and having a thickness equal to the equivalent-area-reduction thickness of the roughness sheets were installed in the shock tube ahead of the measurement section. In view of this like result, it is felt that the 12-percent area reduction due to the roughness does not appreciably affect the attenuation results; this result is probably due to the fact that the full shock-tube area is again attained at the measurement section. The number  $\frac{4A}{D}$  which appears in the shock-pressure-attenuation coefficient is the hydraulic diameter of the shock tube and the value appropriate to the results obtained when smooth or rough sheets were installed is, of course, smaller than the actual shock-tube hydraulic diameter.

It can be seen in figure 15 that there is good agreement of the results with the simple theoretical concept used within the scatter of the data. However, the experimental scatter is such as to disallow a conclusive comparison. It can be seen in figures 16 to 19 that the agreement of the rough-wall results with the simple theory generally is good at the lower values of shock-pressure ratio but is increasingly poorer at the higher pressure ratios as the roughness height increases and as the roughness length increases.

#### Pipe-Flow Effect

Since the roughness covers all four walls of the shock tube and since the boundary layer does theoretically reach the center of the shock tube in a substantial part of the range of conditions covered, a pipe-flow effect is suggested; that is, as the ratio of  $\delta$  to the shock-tube half-width  $\frac{b}{2}$  approaches unity, the theoretical concepts which were used would be increasingly less applicable. The ratio  $\frac{2\delta}{b}$  (or  $\frac{2\delta^*}{b}$ ) increases with shock-pressure ratio, roughness size, and roughness length. In order to see whether any such pipe-flow effect is present, the data are shown in figure 20 as a ratio of experimental to theoretical attenuation plotted as a function of  $\frac{2\delta^*}{b}$ . The arrow indicates the abscissa at which  $\delta = \frac{1}{2}b$  and to the right of which would be the pipe-flow regime.

It can be seen from figure 20 that the data are generally less in agreement with the simple theory at the larger values of  $\frac{2\delta^*}{b}$ . The agreement of the data and theory for the high-pressure-ratio ends of the curves (right ends) appears to be very definitely a function of the displacement-thickness parameter. This statement might also be said of the low-pressure-ratio data (that to the left) except for that obtained with the largest roughness. It appears more likely, however, that there



is a pressure-ratio effect in addition to the effect of displacement thickness on the agreement of the results. There is a definite difference in the nature of the pressure records for the high-pressure-ratio shocks and for the low values. In figure 21 is shown the pressure record obtained with configuration 7 for each of these cases. The pressure following the shock is seen to rise gradually with time in the case of the low-pressure ratio and to fall with time in the case of high pressure ratio.

### Qualification of Results

In drawing any conclusions from the results which have been obtained from boundary-layer measurements and shock-attenuation measurements, certain points must be kept in mind. The boundary-layer thickness  $\delta$  for the unsteady-flow pyramid roughness agreed well with both the steady-flow sand-roughness theory and the steady-flow measurements for sand roughness and lateral square-bar roughness. The velocity profiles for the unsteady-flow pyramid-roughness cases agreed well with the steady-flow lateral-bar cases when equation (6) was used but did not agree with the commercial sand-roughness case or the Schlichting sand theory. It cannot be concluded whether the agreement of the pyramid and lateral-bar data is due to the difference in roughness form being offset by the difference in the steady and unsteady flow or whether the two forms are equally different from sand and there is no difference due to the time nature of the flows. This question could best be settled, of course, by steady-flow boundary-layer measurements using pyramid roughness by methods similar to those used in reference 15. It should be remembered when any comparison of the data shown is made with the theory that the Nikuradse profiles were obtained in pipes and represent streamwise pressure gradients whereas the other cases represent little or no pressure gradient.

In any case, examination of equation (19) and figure 11 shows that the effect of these differences in velocity profiles on the parameter  $\frac{\theta}{x}$  and hence  $C_f$  (see eq. (11)) is not large.

The effect of velocity-profile differences on the boundary-layer displacement thickness (and hence on shock attenuation), however, is more pronounced, as can be seen from figure 11 and equation (29). This effect is also seen in figure 4 where the values of the boundary-layer parameters  $\frac{\theta}{\delta}$  and  $\frac{\delta^*}{\delta}$  that result from integration of the experimental profiles are shown. Therefore, the equivalence of an arbitrary roughness to sand roughness on the basis of equal friction is not sufficient for equivalence of the displacement thickness. It would be expected from this result that the attenuation theory which has been presented would predict values of attenuation which are too low. However, quantitative refinement is not warranted in view of some of the other assumptions made in the simple theory. These assumptions include:

incompressible flow, constant velocity distribution along the surface, no wall heat transfer, a Prandtl number of 1, and use of boundary-layer characteristics at only the entropy discontinuity station to describe the attenuation.

#### CONCLUDING REMARKS

Measurements of unsteady-flow turbulent boundary-layer characteristics using the bullet technique and shock-wave attenuation in the shock tube with pyramid-shaped surface roughness and subsequent comparisons with steady-flow theory lead to the following conclusions:

1. Good agreement of the boundary-layer-thickness measurements with flat-plate steady-flow sand-roughness theory and with steady-flow data using both sand roughness and lateral square bars was obtained.

2. Measurements of the boundary-layer velocity profiles show a considerably less full profile than the steady-flow sand-roughness theoretical profile but agreed well with steady-flow profiles for lateral square-bar roughness. It is shown that these differences in velocity profiles do not lead to large differences in momentum thickness but lead to much larger differences in the displacement thicknesses.

3. Shock-wave-attenuation measurements agreed reasonably well with a simple attenuation theory for small values of boundary-layer displacement thickness, but the measurements were considerably lower than theory at the higher values of displacement thickness.

Langley Aeronautical Laboratory,  
National Advisory Committee for Aeronautics,  
Langley Field, Va., December 12, 1955.

## REFERENCES

1. Glass, I. I., Martin, W., and Patterson, G. N.: A Theoretical and Experimental Study of the Shock Tube. UTIA Rep. No. 2, Inst. of Aerophysics, Univ. of Toronto, Nov. 1953.
2. Hollyer, Robert N., Jr.: A Study of Attenuation in the Shock Tube. Proj. M720-4 (Contract N6-ONR-232-TO IV, Office of Naval Res.), Univ. of Michigan Eng. Res. Inst., July 1, 1953.
3. Mack, John E.: Density Measurement in Shock Tube Flow With the Chrono-Interferometer. Tech. Rep. 4, Lehigh Univ. Inst. Res. (Proj. NR-061-063, Contract N7onr39302; Office of Naval Res.), Apr. 15, 1954.
4. Trimpf, Robert L., and Cohen, Nathaniel B.: A Theory for Predicting the Flow of Real Gases in Shock Tubes With Experimental Verification. NACA TN 3375, 1955.
5. Donaldson, Coleman duP., and Sullivan, Roger D.: The Effect of Wall Friction on the Strength of Shock Waves in Tubes and Hydraulic Jumps in Channels. NACA TN 1942, 1949.
6. Lobb, R. K.: A Study of Supersonic Flows in a Shock Tube. UTIA Rep. No. 8, Inst. of Aerophysics, Univ. of Toronto, May 1950.
7. Emrich, R. J., and Curtis, C. W.: Attenuation in the Shock Tube. Jour. Appl. Phys., vol. 24, no. 3, Mar. 1953, pp. 360-363.
8. Mirels, Harold: Laminar Boundary Layer Behind Shock Advancing Into Stationary Fluid. NACA TN 3401, 1955.
9. Crocco, Luigi: Transmission of Heat From a Flat Plate to a Fluid Flowing at a High Velocity. NACA TM 690, 1932.
10. Schlichting, H.: Lecture Series "Boundary Layer Theory." Part II - Turbulent Flows. NACA TM 1218, 1949.
11. Von Kármán, Th.: Turbulence and Skin Friction. Jour. Aero. Sci., vol. 1, no. 1, Jan. 1934, pp. 1-20.
12. Nikuradse, J.: Laws of Flow in Rough Pipes. NACA TM 1292, 1950.
13. Schlichting, H.: Experimental Investigation of the Problem of Surface Roughness. NACA TM 823, 1937.

14. Klebanoff, P. S., and Diehl, Z. W.: Some Features of Artificially Thickened Fully Developed Turbulent Boundary Layers With Zero Pressure Gradient. NACA Rep. 1110, 1952. (Supersedes NACA TN 2475.)
15. Moore, Walter L.: An Experimental Investigation of the Boundary-Layer Development Along a Rough Surface. Ph.D. Dissertation, Univ. of Iowa, 1951.

TABLE I.- CONFIGURATION OF LOW-PRESSURE SIDE OF SHOCK TUBE (HIGH-PRESSURE

SIDE - 4 FEET LONG IN ALL CASES)

[Air-to-air room temperature]

Number	Configuration	Roughness condition	k, in.	Distance from diaphragm, ft				
				Smooth wall	Rough wall	Window section	Shock velocity measurement section	l
1	Bullet	Roughness on bottom wall only	0.25	0 to 10	10 to 16	12 to 14	8 to 10	$x_{TW} \approx 3$
2	Bullet	Roughness on bottom wall only	.25	0 to 14	14 to 16	14 to 16	12 to 14	$x_{TW} \approx 1$
3	Smooth-wall attenuation	-----		0 to 14	-----	-----	12 to 14	13
4	Rough-wall attenuation	Roughness on all four walls	.0625	0 to 8 and 12 to 14	8 to 12	-----	12 to 14	5
5	Rough-wall attenuation	Roughness on all four walls	.125	0 to 12 and 16 to 18	12 to 16	-----	16 to 18	5
6	Rough-wall attenuation	Roughness on all four walls	.125	0 to 4 and 12 to 14	4 to 12	-----	12 to 14	9
7	Rough-wall attenuation	Roughness on all four walls	.25	0 to 4 and 12 to 14	4 to 12	-----	12 to 14	9

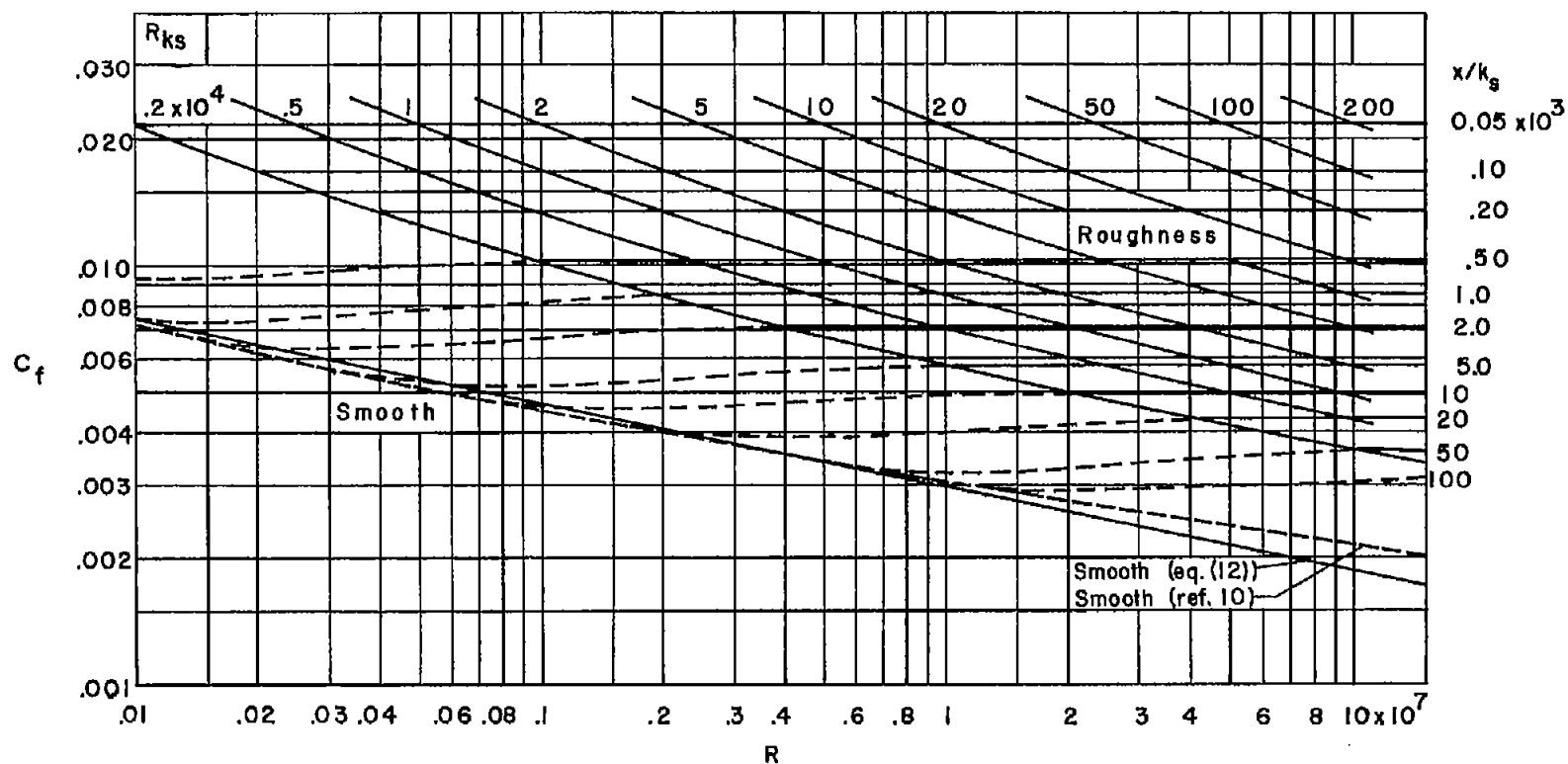


Figure 1.- Turbulent total-skin-friction coefficients for the smooth flat plate and the sand-roughened flat plate for incompressible flow according to Schlichting (ref. 10). Dashed region indicates the roughness flow which is not fully developed.

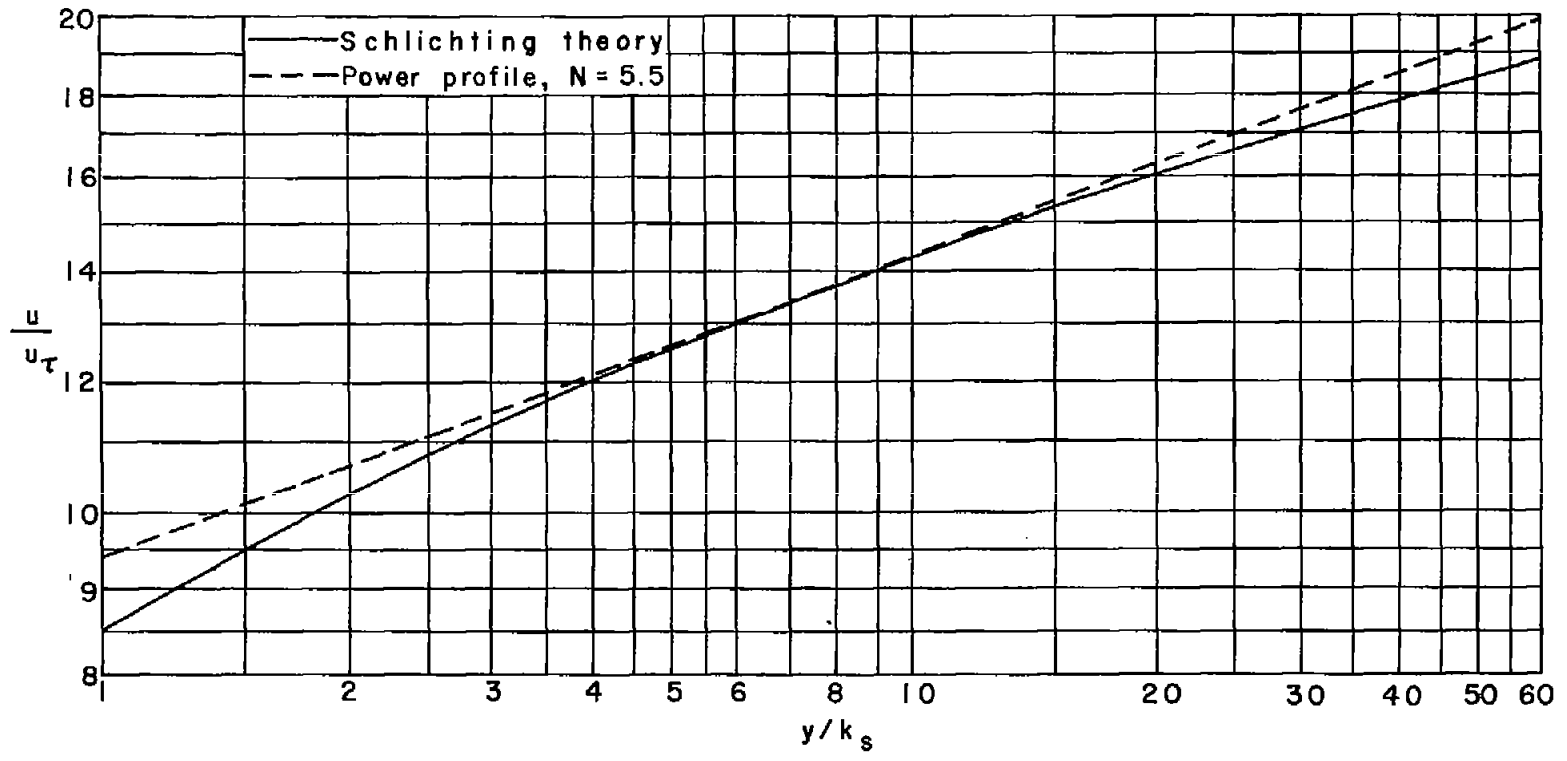


Figure 2.- Boundary-layer-velocity distribution for fully developed sand-roughness flow according to Schlichting (ref. 10).

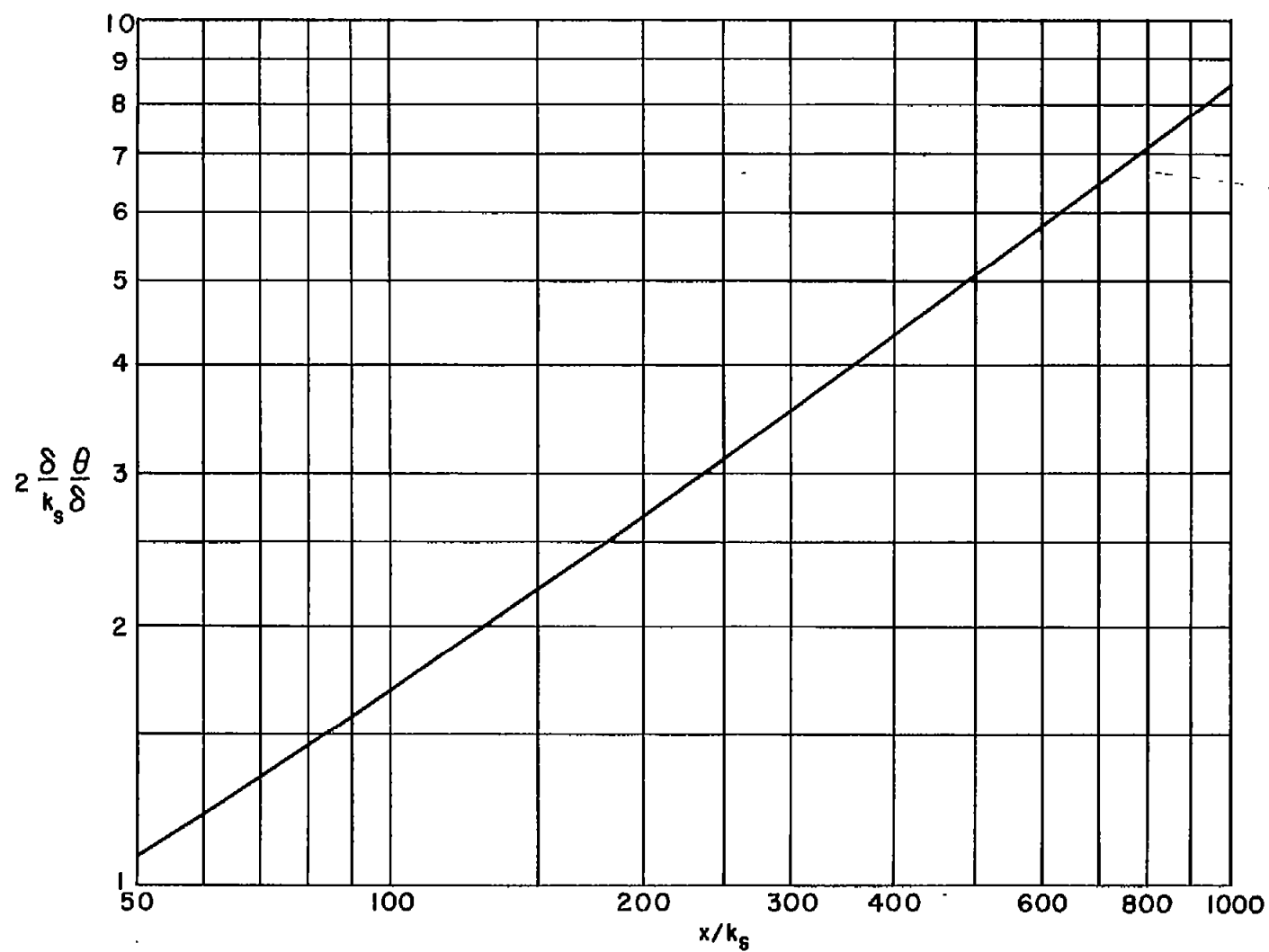


Figure 3.- Theoretical growth of boundary-layer momentum thickness along a plate for fully developed sand-roughness flow.



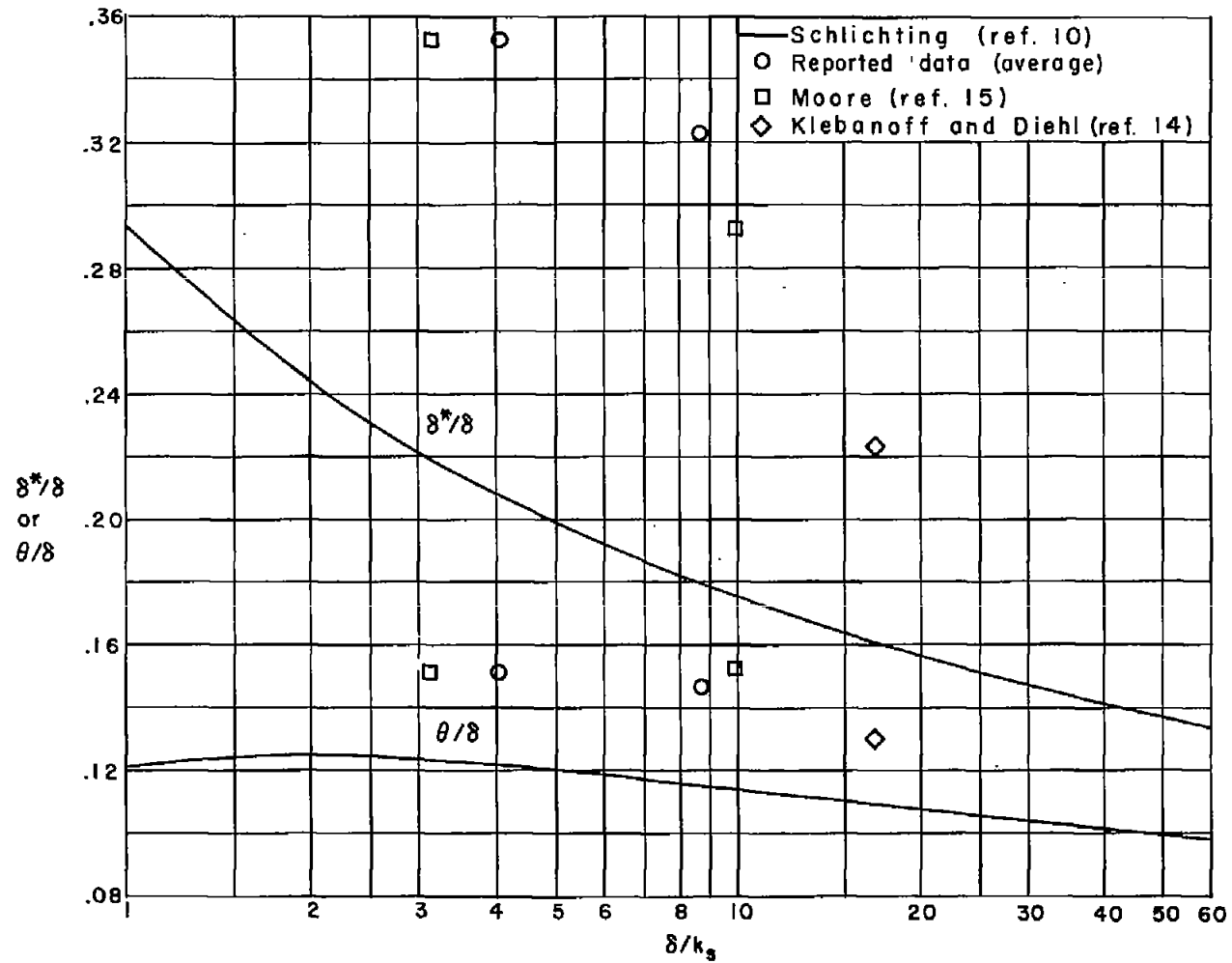


Figure 4.- Comparison of theoretical and experimental dependency of the boundary-layer parameters on the boundary-layer thickness for fully developed roughness flow.

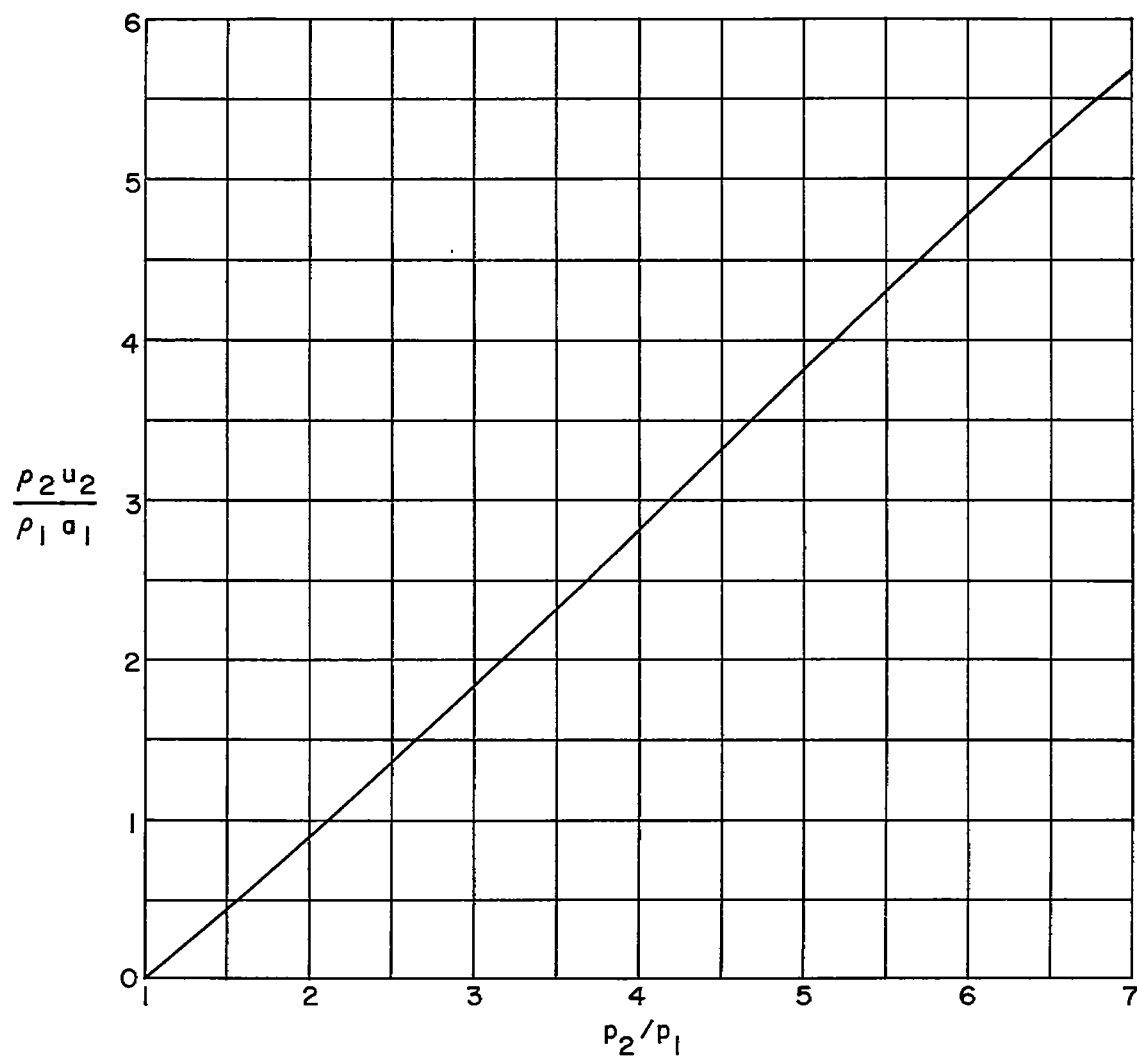
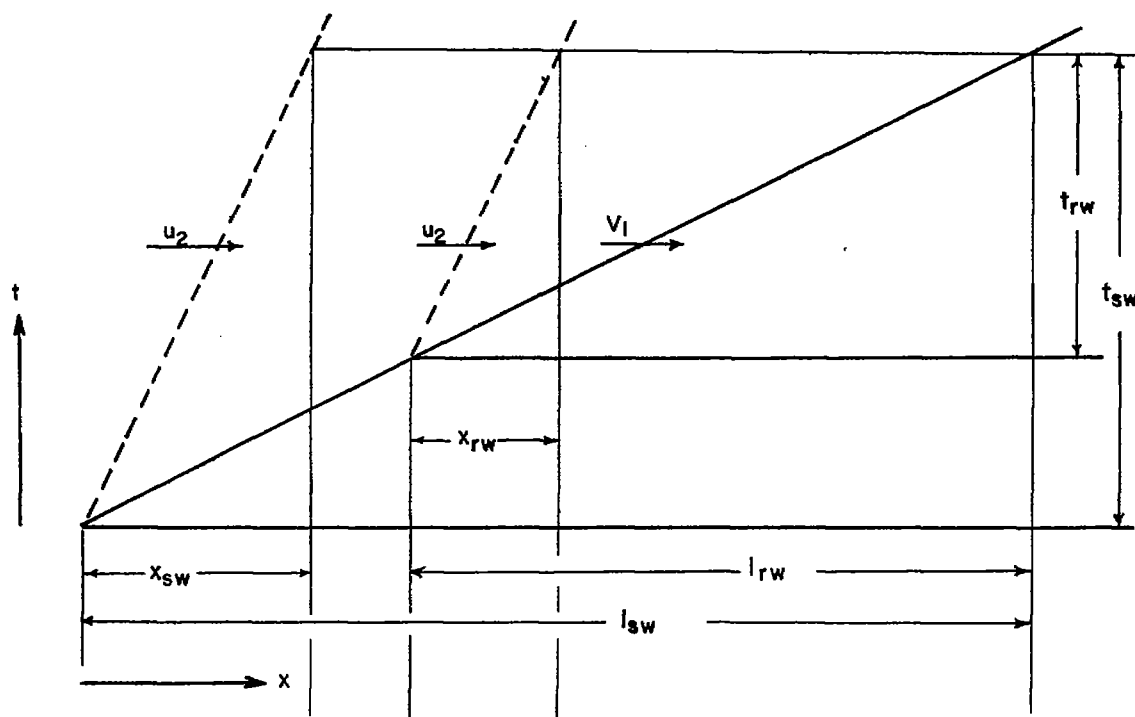
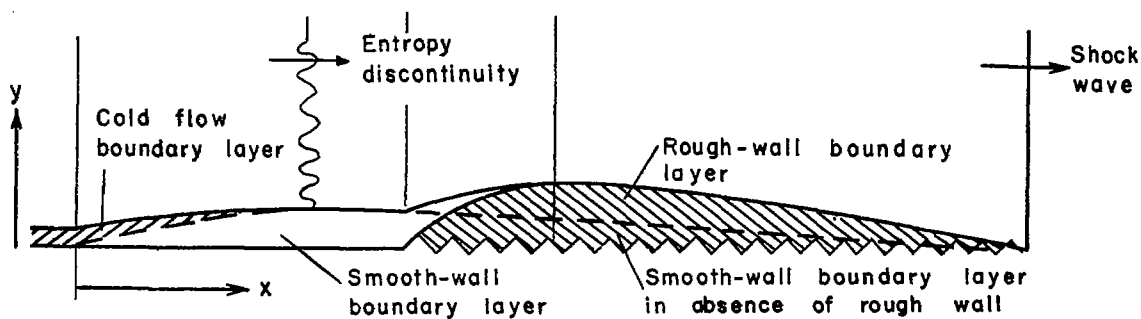


Figure 5.- Mass flow per unit area accelerated by a shock wave moving into a stationary fluid as a function of shock strength.



(a) Shock tube  $x - t$  diagram for low-pressure side showing the flow lengths appropriate to the smooth-wall and rough-wall flow.



(b) Physical representation of boundary-layer growth along shock tube at time  $t_{sw}$ .

Figure 6.- Shock-tube flow representations.

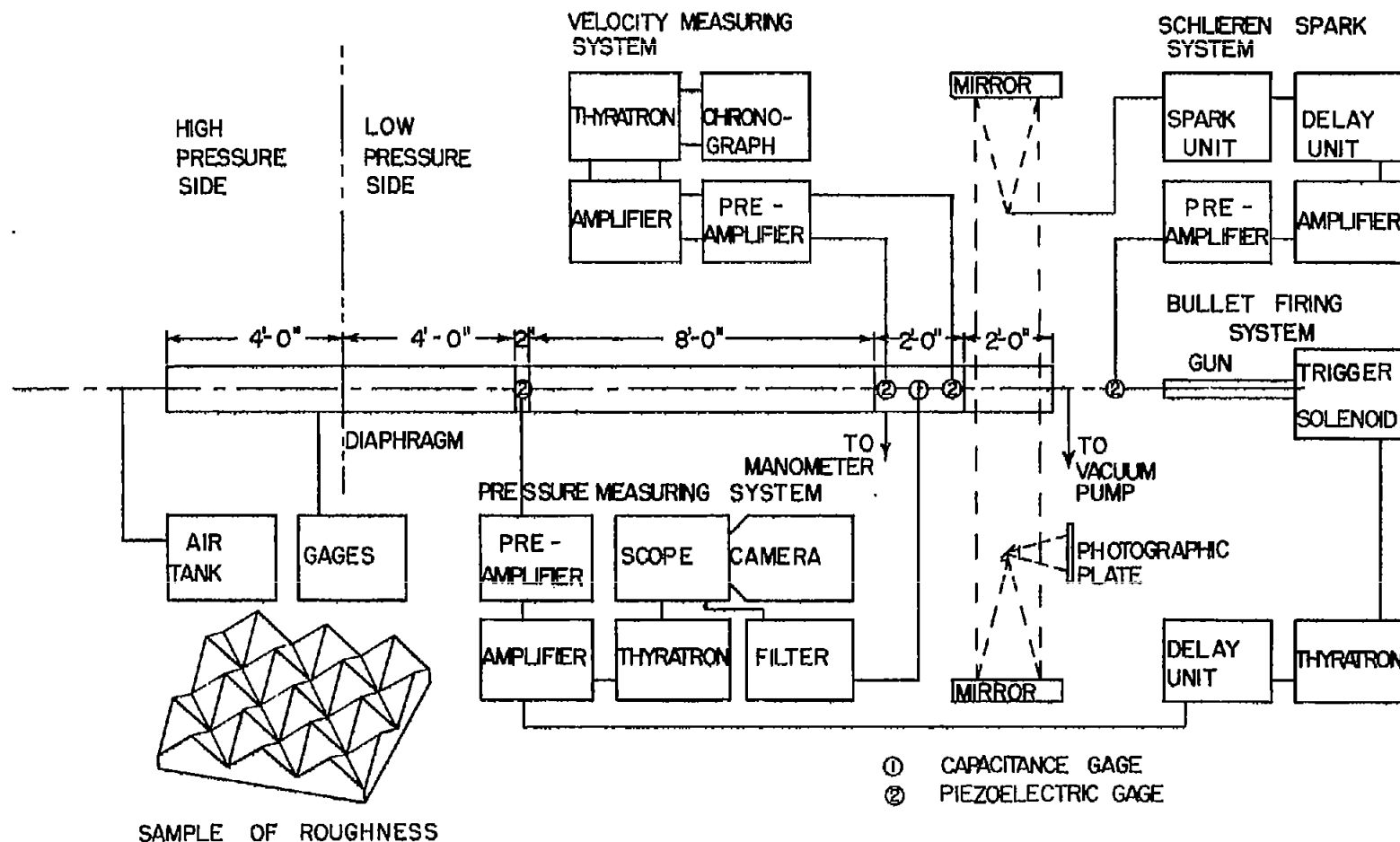


Figure 7.- Schematic arrangement of shock tube and instrumentation.



(a) Bullet bow-wave distortion at the rough wall.



(b) Reflections of the shock from the roughness elements. L-91694

Figure 8.- Schlieren photographs typical of those obtained for the roughness conditions.

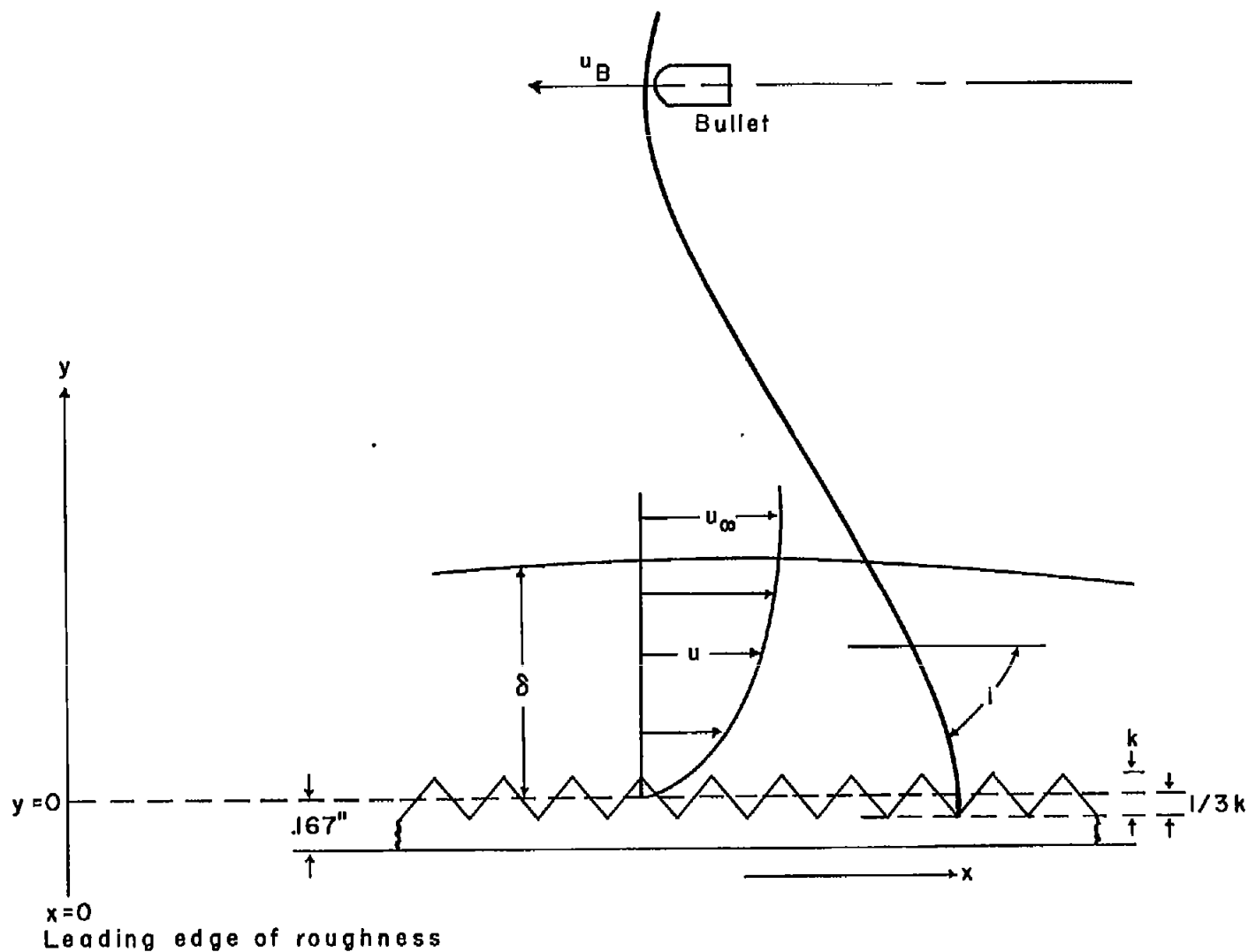


Figure 9.- Application of the bullet technique to rough-wall boundary-layer measurements showing location of coordinates used.

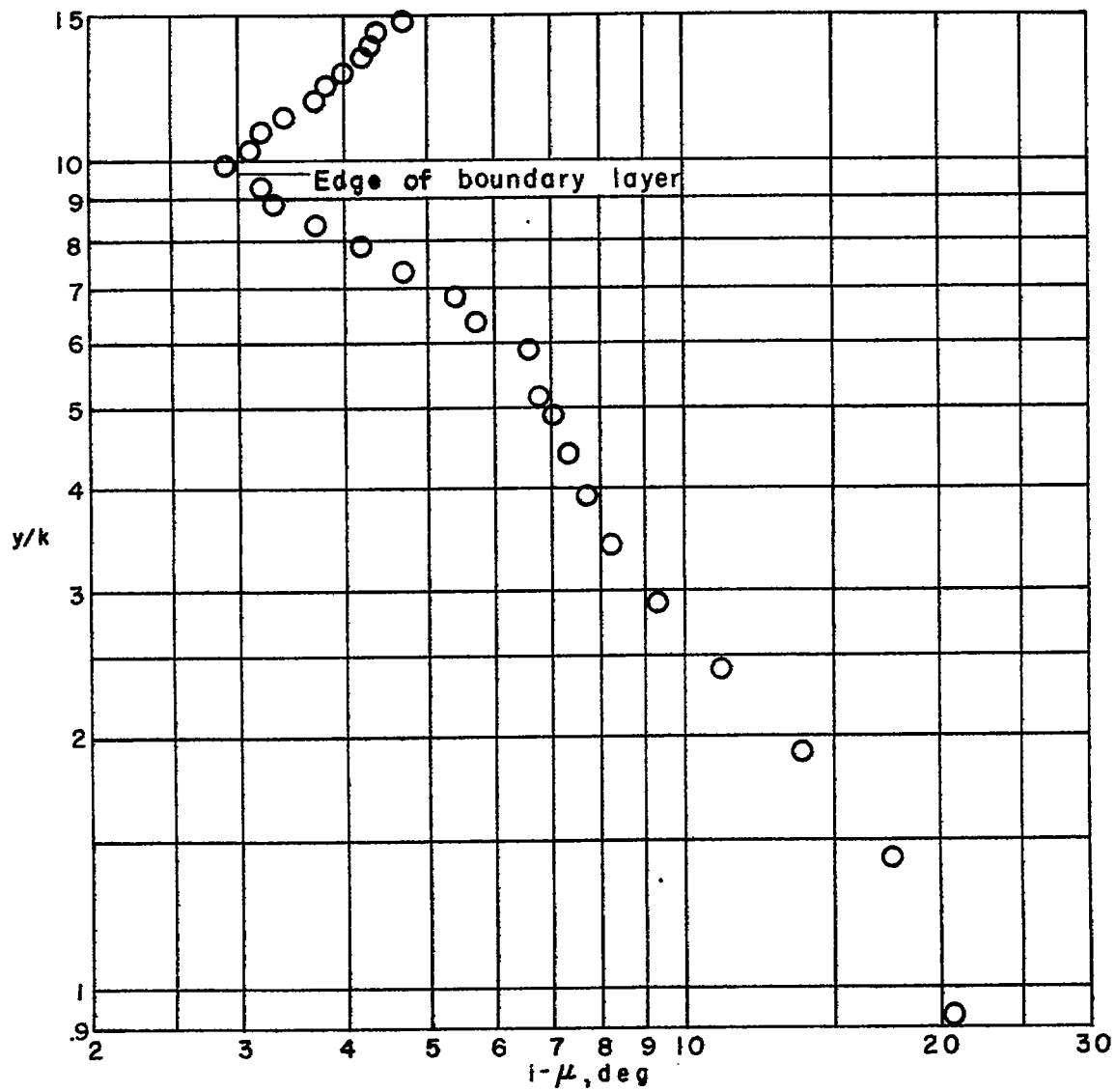


Figure 10.- Measurements of the bullet bow-wave incidence angle minus Mach angle through the boundary layer on a rough wall.  $M_2 = 1.55$ .

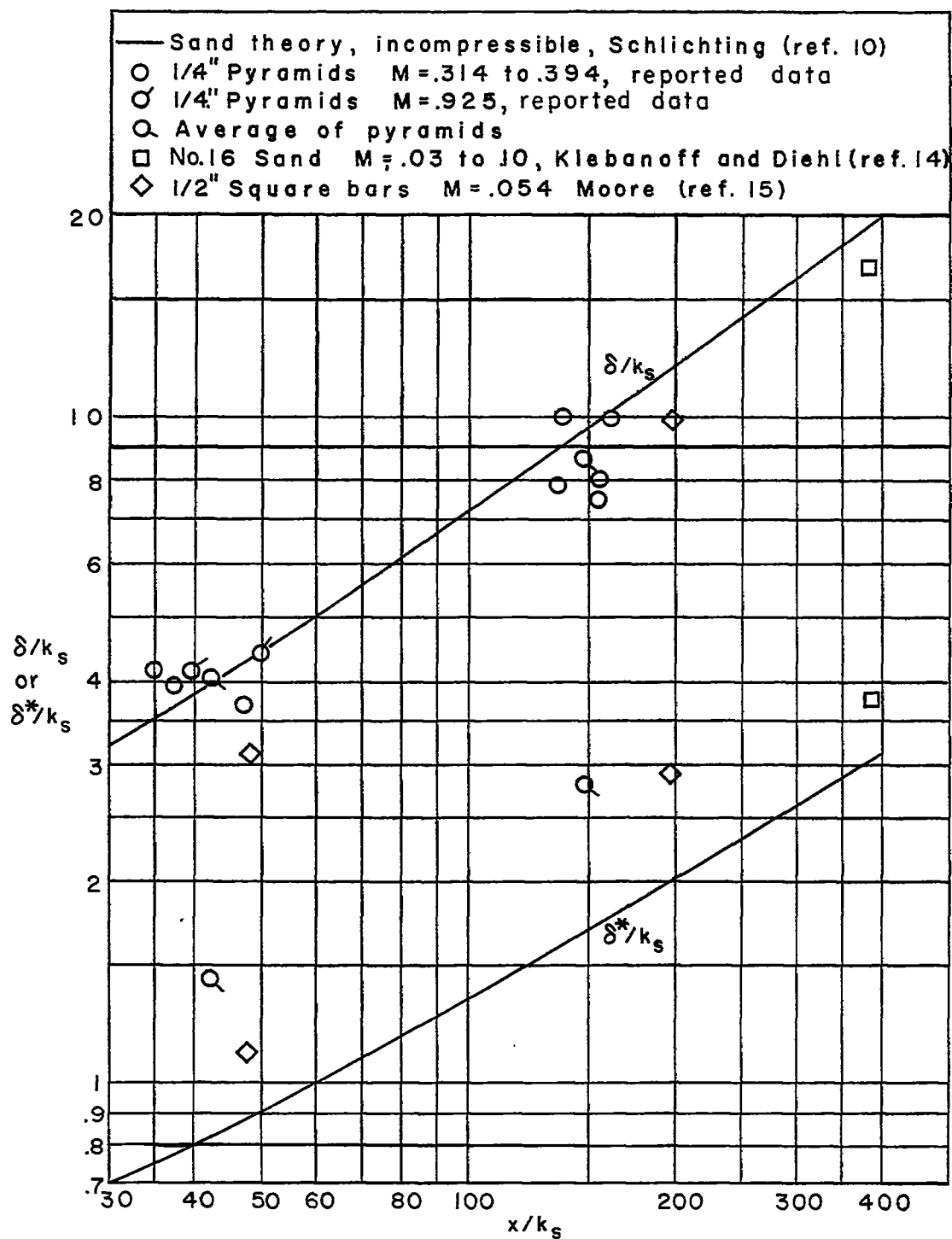


Figure 11.- Comparison of experimental and theoretical boundary-layer thickness and displacement thickness along a rough plate for unsteady and steady flow.



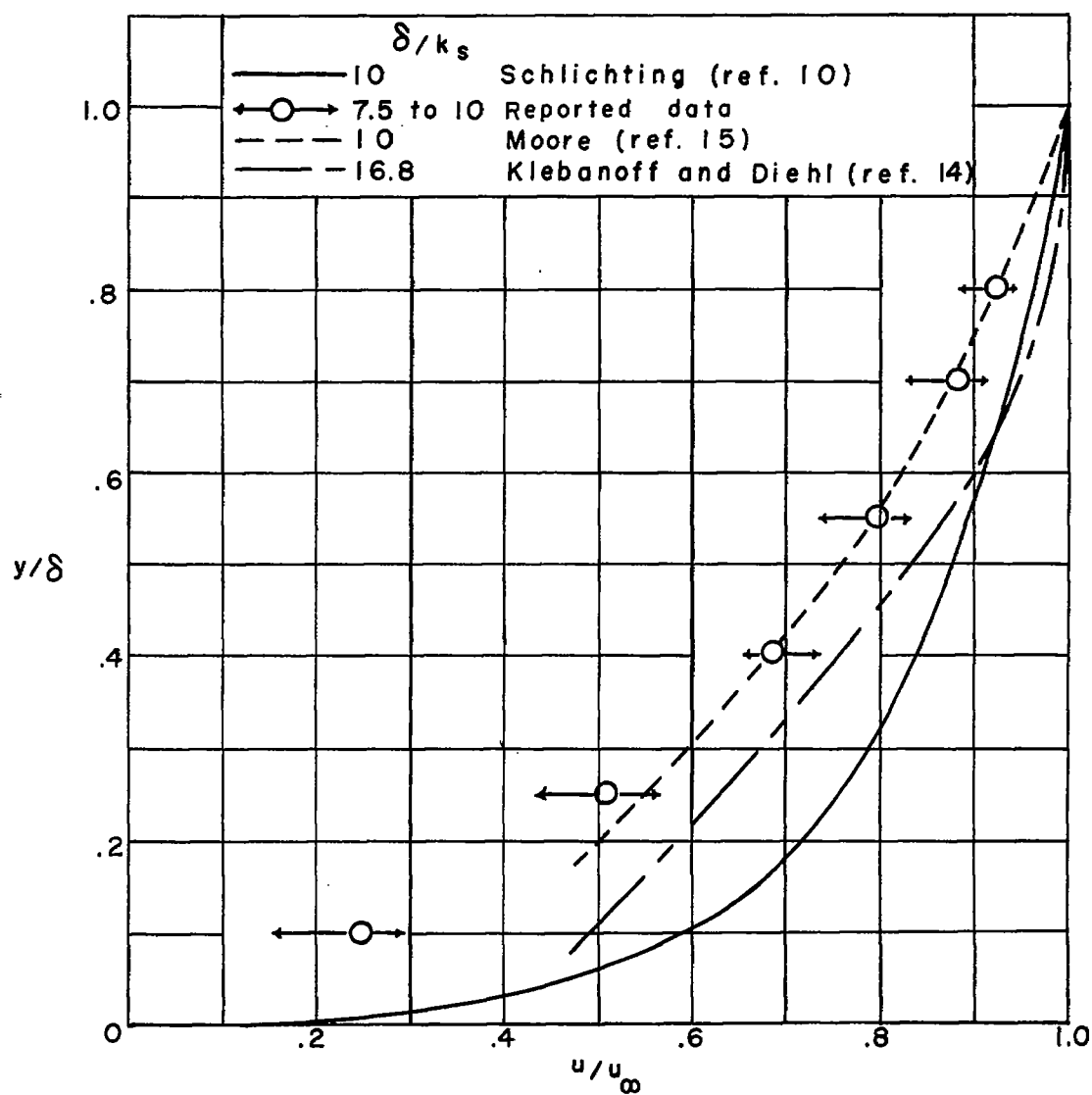


Figure 12.- Comparison of experimental and theoretical boundary-layer velocity distribution for unsteady and steady roughness flow.  
 $\delta/k_s \approx 10$ .

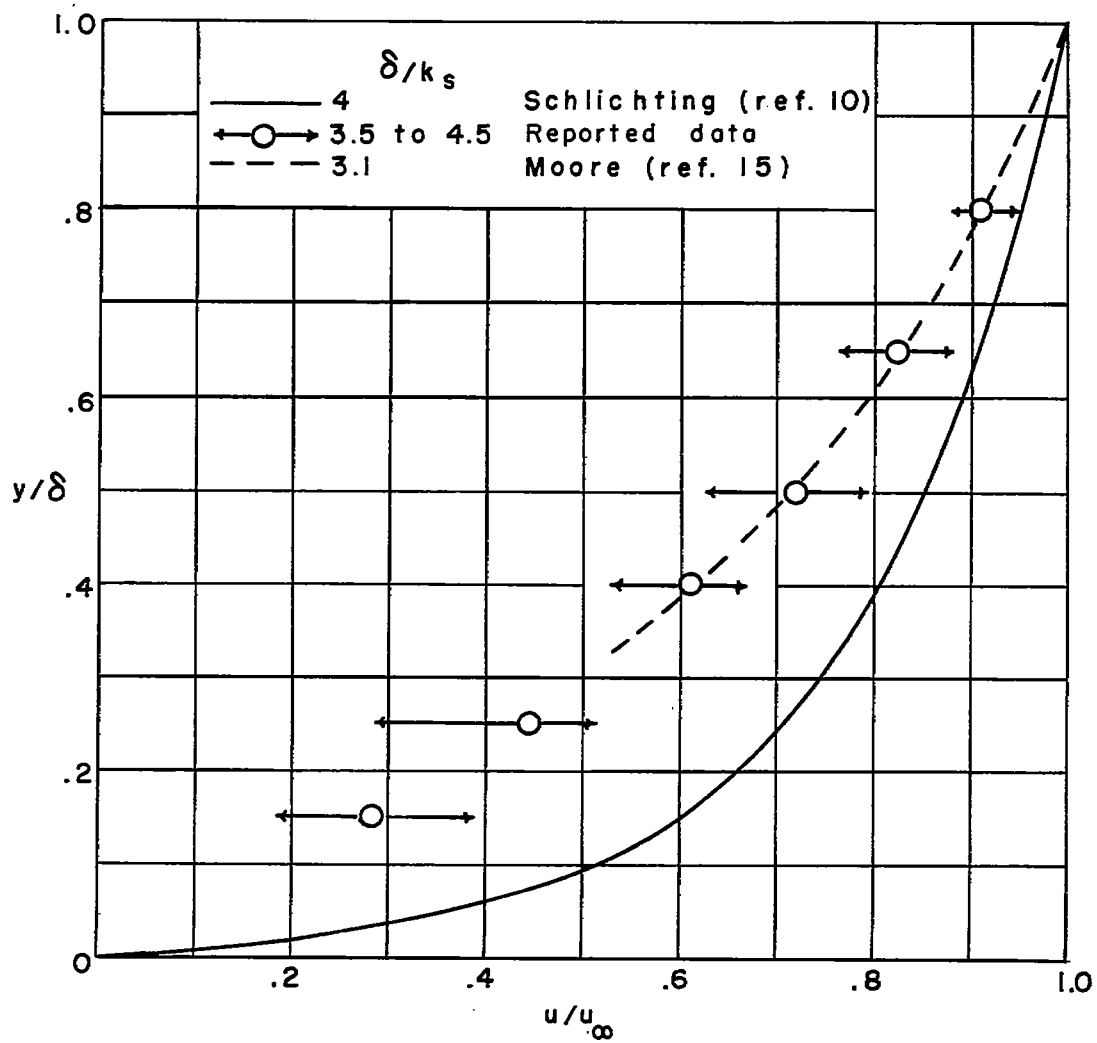


Figure 13.- Comparison of experimental and theoretical boundary-layer velocity distribution for unsteady and steady roughness flow.  
 $\delta/k_s \approx 4$ .

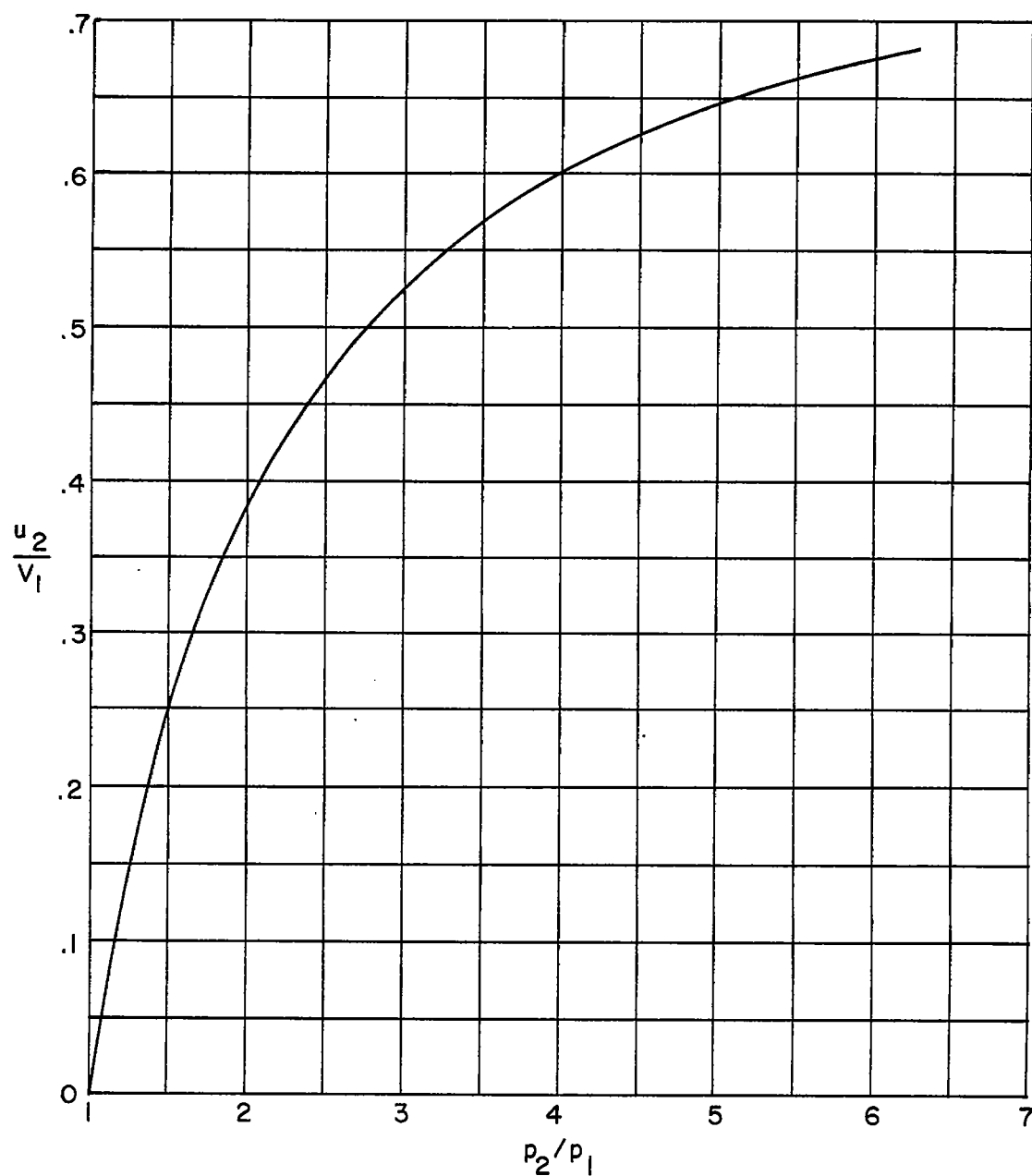


Figure 14.- Theoretical ratio of fluid velocity to shock-wave velocity as a function of shock-wave strength for a shock wave moving into a stationary fluid.  $\gamma = 1.40$ .

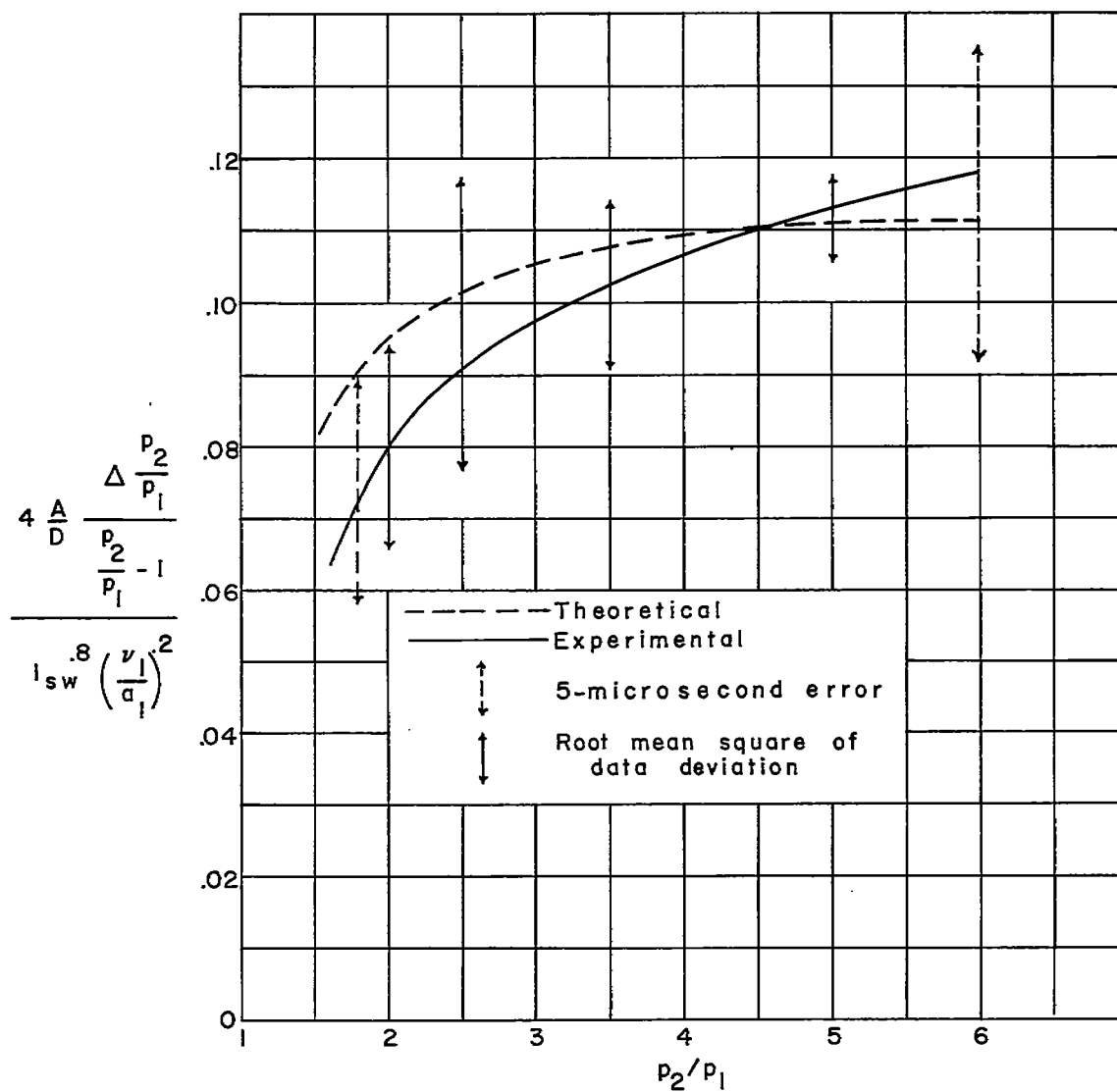


Figure 15.- Comparison of theoretical and experimental shock-pressure attenuation coefficient as a function of shock strength for smooth-wall flow.  $l_{sw} = 13$  feet.

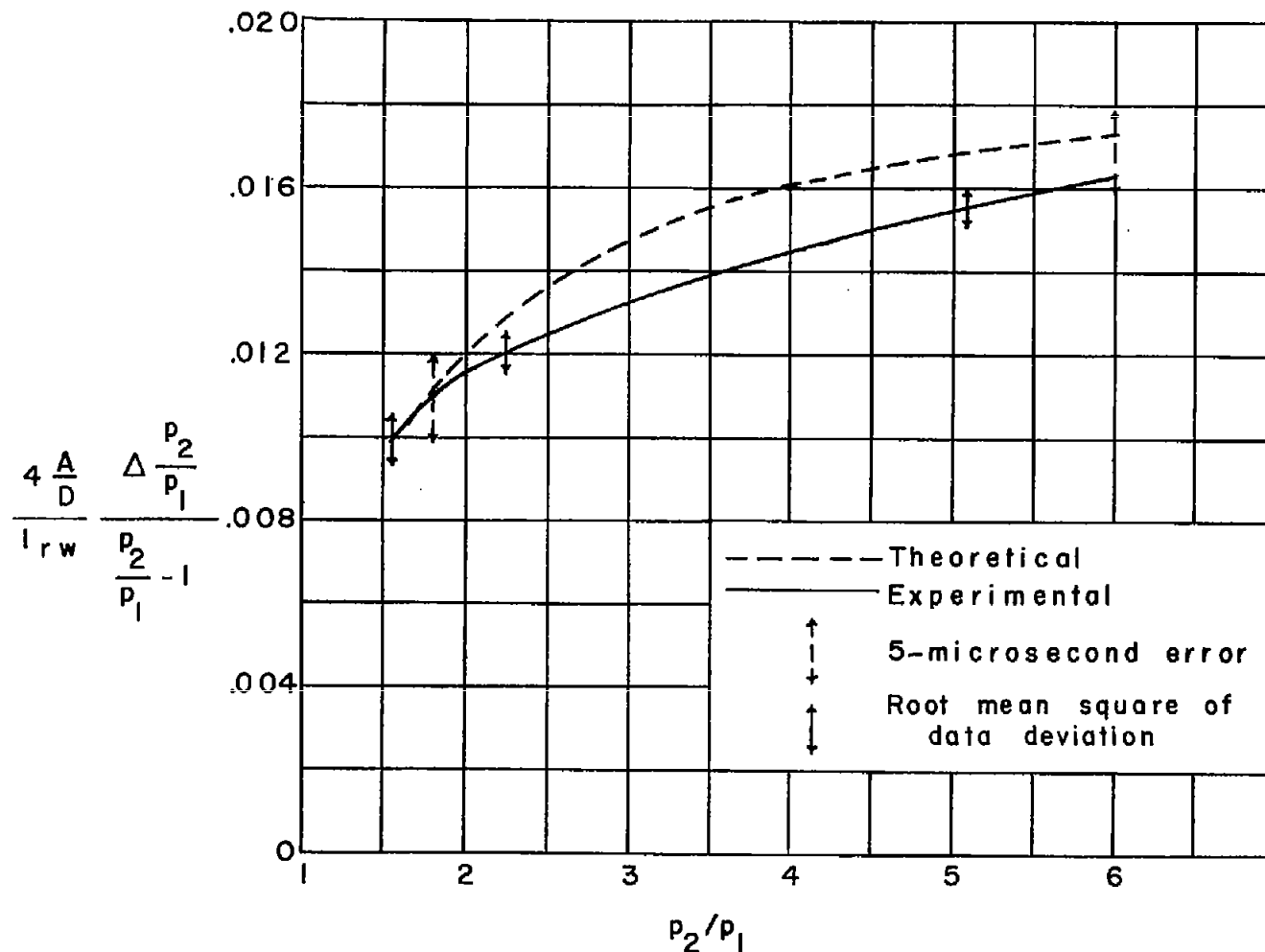


Figure 16.- Comparison of theoretical and experimental shock-pressure attenuation coefficient as a function of shock strength for roughness flow.  $l_{rw}/k_g = 1,080$ ;  $l_{rw} = 5$  feet.

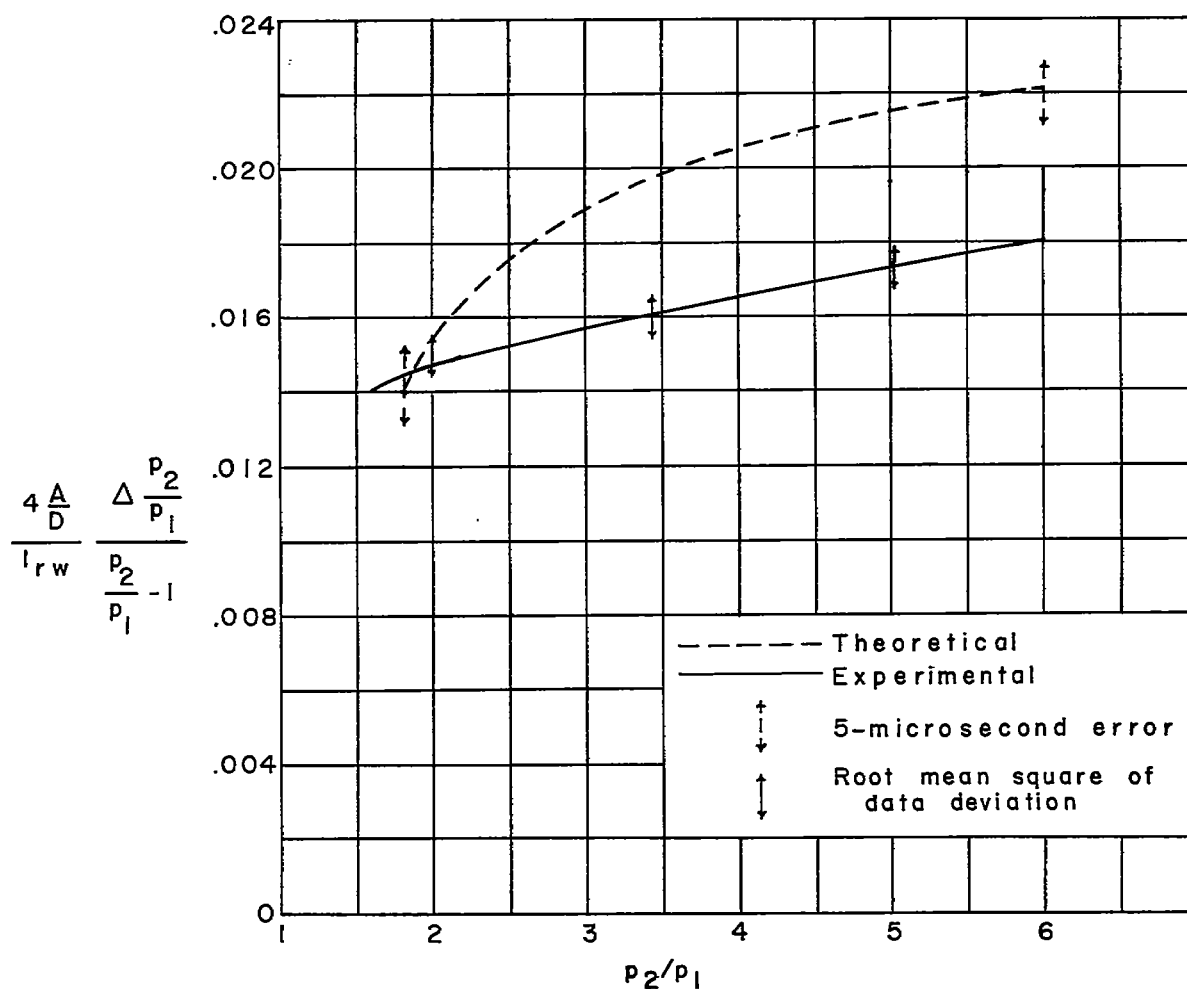


Figure 17.- Comparison of theoretical and experimental shock-pressure attenuation coefficient as a function of shock strength for roughness flow.  $l_{rw}/k_s = 540$ ;  $l_{rw} = 5$  feet.

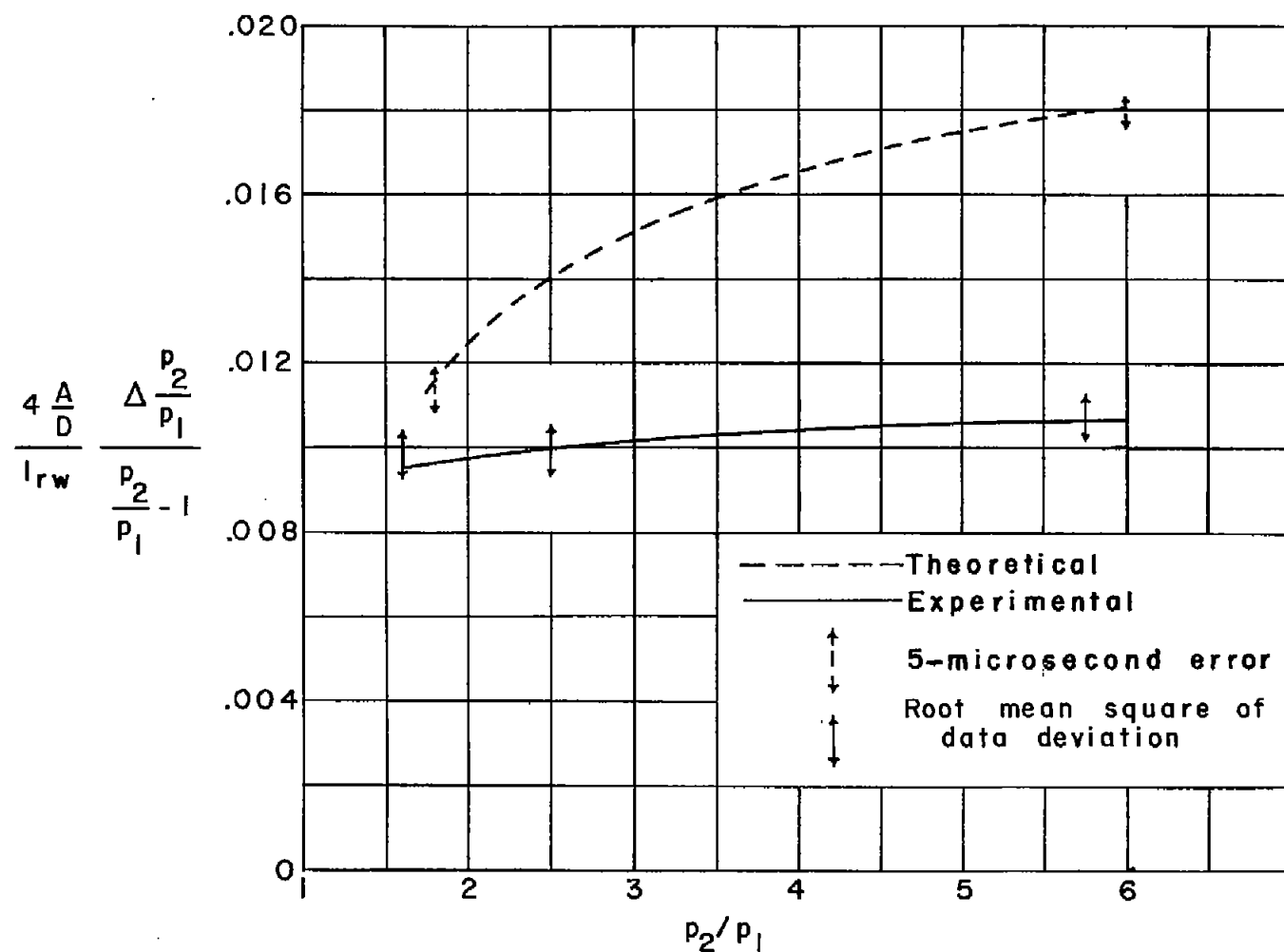


Figure 18.- Comparison of theoretical and experimental shock-pressure attenuation coefficient as a function of shock strength for roughness flow.  $l_{rw}/k_s = 972$ ;  $l_{rw} = 9$  feet.

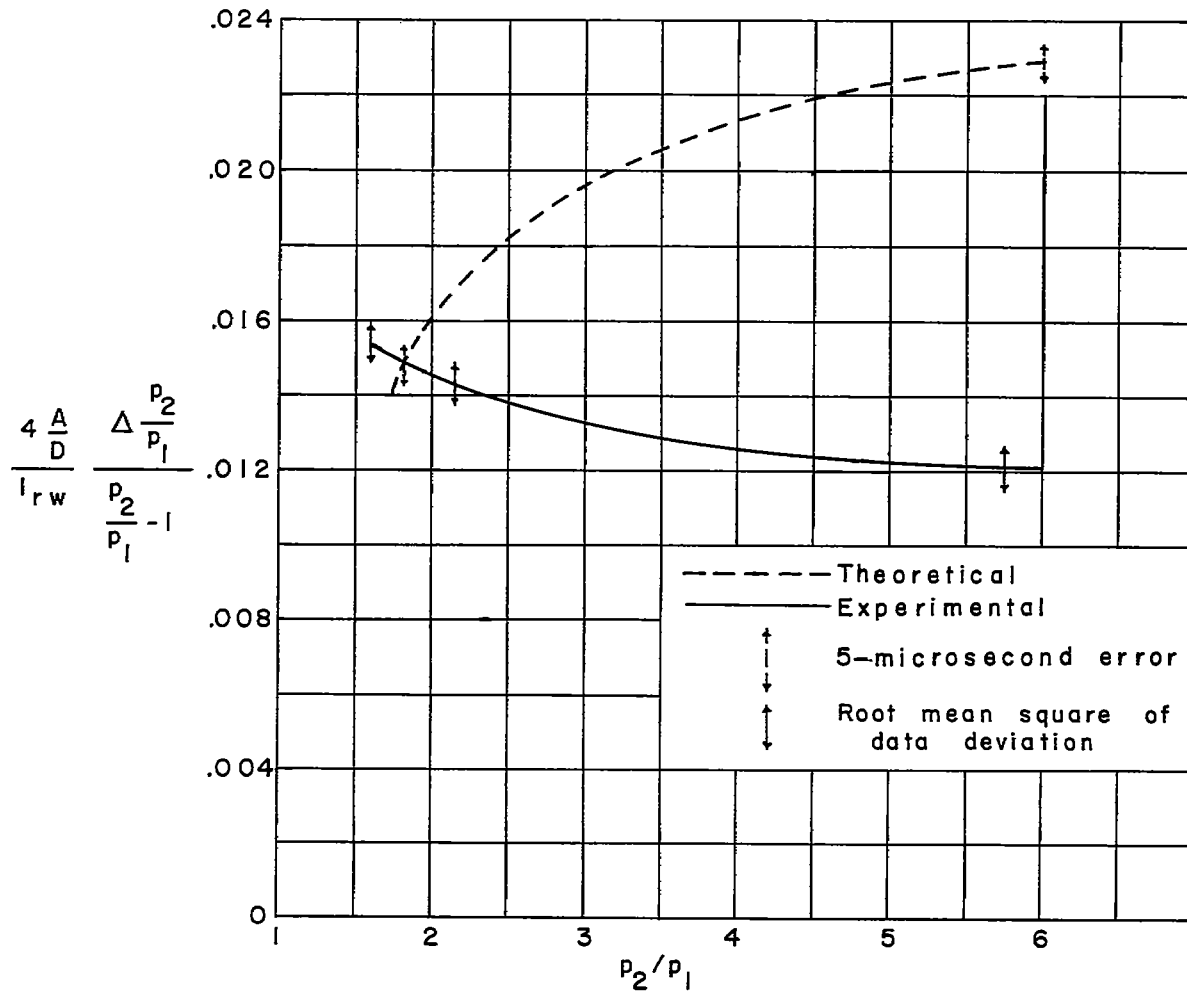


Figure 19.- Comparison of theoretical and experimental shock-pressure attenuation coefficient as a function of shock strength for roughness flow.  $l_{rw}/k_s = 486$ ;  $l_{rw} = 9$  feet.



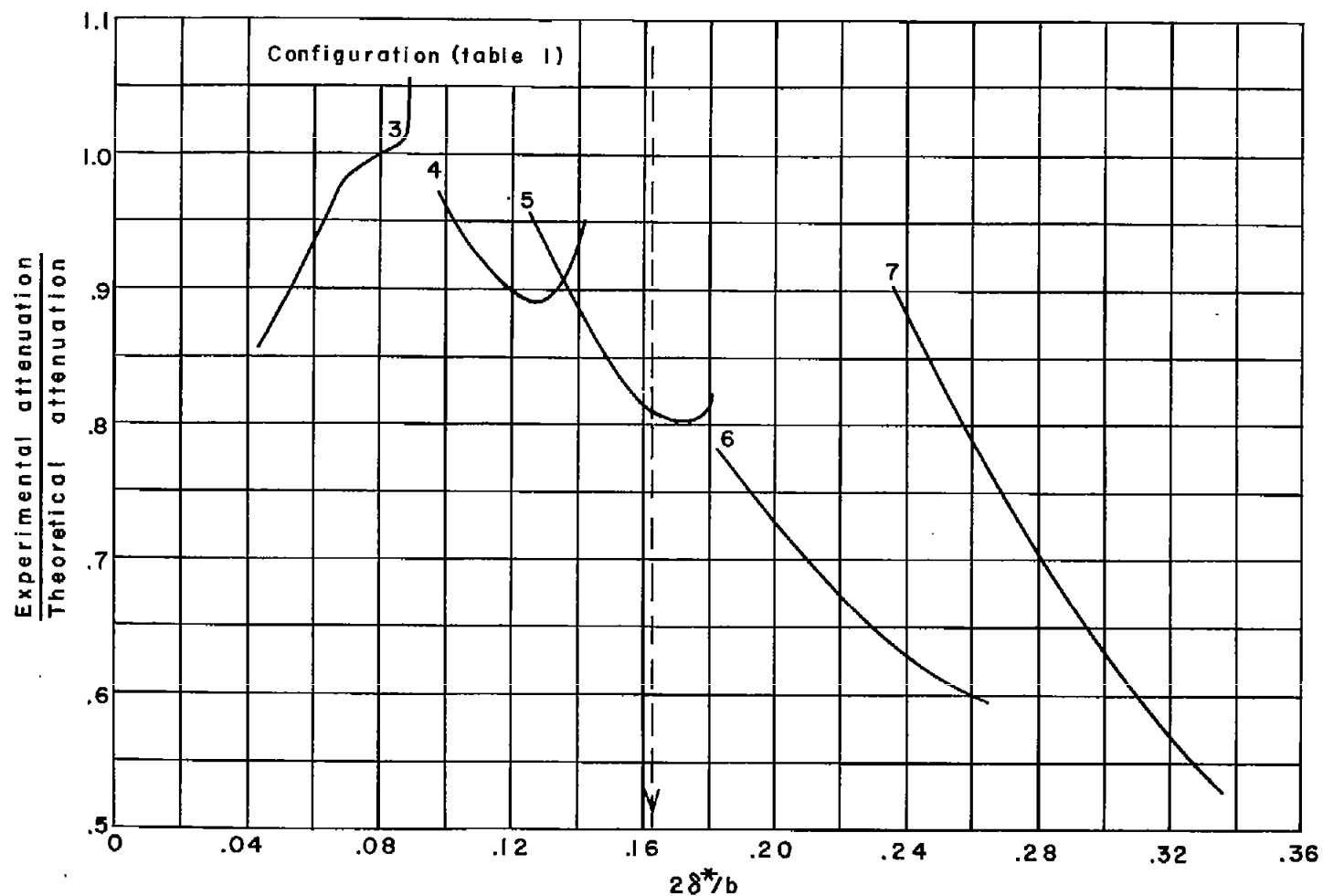
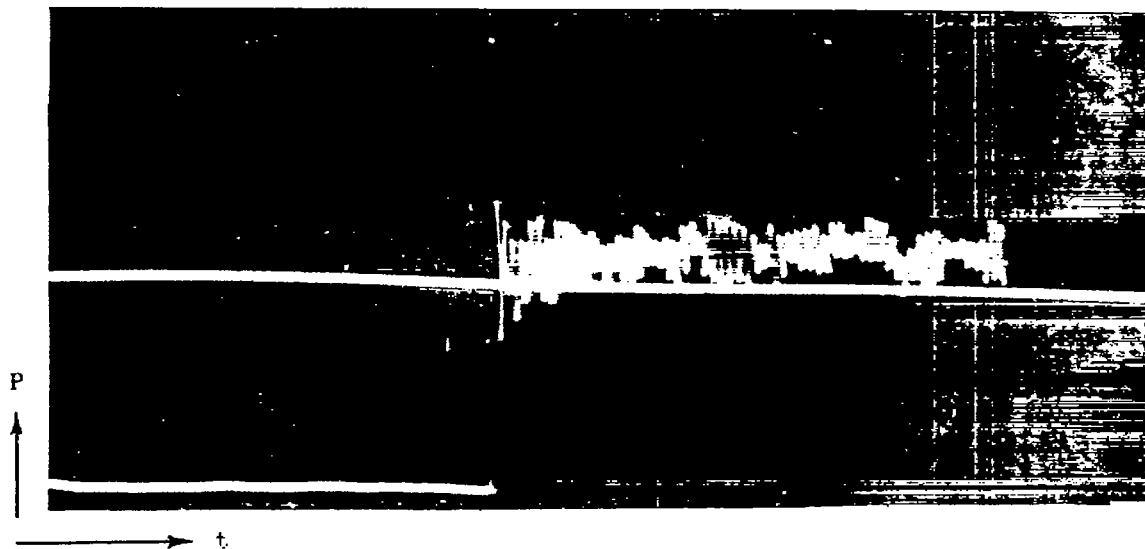
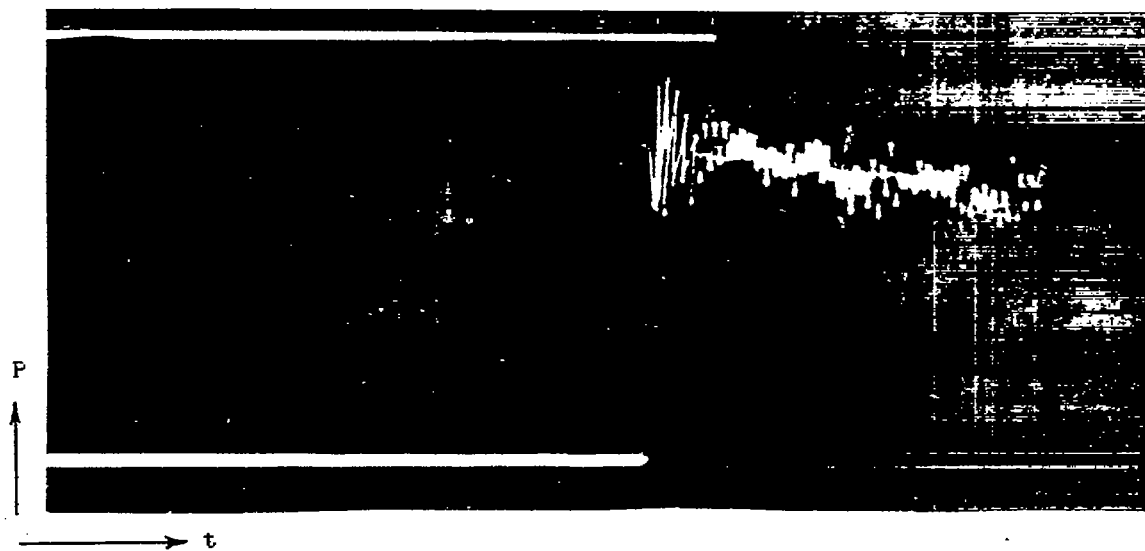


Figure 20.- Ratio of experimental to theoretical shock-wave attenuation as a function of the ratio of boundary-layer displacement thickness to shock-tube half-width. Arrow indicates abscissa at which boundary layer theoretically fills the shock tube.



(a) Weak shock.  $p_2/p_1 = 1.61$ .



(b) Strong shock.  $p_2/p_1 = 5.54$ .

L-80228.1

Figure 21.- Typical records of the variation of pressure with time of shocks after traveling over roughness. Configuration 7.